



Universiteit
Leiden
The Netherlands

EMPRESS. IV. Extremely metal-poor galaxies including very low-mass primordial systems with $M^* = 10^4$ - 10^5 M and 2%-3% (O/H) high (Fe/O) suggestive of metal enrichment by hypernovae/pair-instability supernovae

Isobe, Y.; Ouchi, M.; Suzuki, A.; Moriya, T.J.; Nakajima, K.; Nomoto, K.; ... ; Xu, Y.

Citation

Isobe, Y., Ouchi, M., Suzuki, A., Moriya, T. J., Nakajima, K., Nomoto, K., ... Xu, Y. (2022). EMPRESS. IV. Extremely metal-poor galaxies including very low-mass primordial systems with $M^* = 10^4$ - 10^5 M and 2%-3% (O/H): high (Fe/O) suggestive of metal enrichment by hypernovae/pair-instability supernovae. *The Astrophysical Journal*, 925(2). doi:10.3847/1538-4357/ac3509

Version: Publisher's Version
License: [Creative Commons CC BY 4.0 license](https://creativecommons.org/licenses/by/4.0/)
Downloaded from: <https://hdl.handle.net/1887/3561808>

Note: To cite this publication please use the final published version (if applicable).



EMPRESS. IV. Extremely Metal-poor Galaxies Including Very Low-mass Primordial Systems with $M_* = 10^4\text{--}10^5 M_\odot$ and 2%–3% (O/H): High (Fe/O) Suggestive of Metal Enrichment by Hypernovae/Pair-instability Supernovae

Yuki Isobe^{1,2}, Masami Ouchi^{1,3,4}, Akihiro Suzuki³, Takashi J. Moriya^{3,5}, Kimihiko Nakajima³, Ken'ichi Nomoto⁴, Michael Rauch⁶, Yuichi Harikane^{1,7}, Takashi Kojima^{1,2}, Yoshiaki Ono¹, Seiji Fujimoto^{1,3,8,9,10}, Akio K. Inoue^{11,12}, Ji Hoon Kim^{13,14}, Yutaka Komiyama^{3,15}, Haruka Kusakabe¹⁶, Chien-Hsiu Lee¹⁷, Michael Maseda¹⁸, Jorjyt Matthee¹⁹, Leo Michel-Dansac²⁰, Tohru Nagao²¹, Themiya Nanayakkara²², Moka Nishigaki¹⁵, Masato Onodera^{13,15}, Yuma Sugahara^{3,11}, and Yi Xu^{1,23}

¹ Institute for Cosmic Ray Research, The University of Tokyo, 5-1-5 Kashiwanoha, Kashiwa, Chiba 277-8582, Japan

² Department of Physics, Graduate School of Science, The University of Tokyo, 7-3-1 Hongo, Bunkyo, Tokyo 113-0033, Japan

³ National Astronomical Observatory of Japan, 2-21-1 Osawa, Mitaka, Tokyo 181-8588, Japan

⁴ Kavli Institute for the Physics and Mathematics of the Universe (WPI), University of Tokyo, Kashiwa, Chiba 277-8583, Japan

⁵ School of Physics and Astronomy, Faculty of Science, Monash University, Clayton, Victoria 3800, Australia

⁶ Carnegie Observatories, 813 Santa Barbara Street, Pasadena, CA 91101, USA

⁷ Department of Physics and Astronomy, University College London, Gower Street, London WC1E 6BT, UK

⁸ Cosmic DAWN Center, Niels Bohr Institute, University of Copenhagen, Jagtvej 128, DK-2200, Copenhagen, Denmark

⁹ Niels Bohr Institute, University of Copenhagen, Lyngbyvej 2, DK-2100, Copenhagen, Denmark

¹⁰ Research Institute for Science and Engineering, Waseda University, 3-4-1 Okubo, Shinjuku, Tokyo 169-8555, Japan

¹¹ Waseda Research Institute for Science and Engineering, Faculty of Science and Engineering, Waseda University, 3-4-1, Okubo, Shinjuku, Tokyo 169-8555, Japan

¹² Department of Physics, School of Advanced Science and Engineering, Faculty of Science and Engineering, Waseda University, 3-4-1 Okubo, Shinjuku, Tokyo 169-8555, Japan

¹³ Subaru Telescope, National Astronomical Observatory of Japan, National Institutes of Natural Sciences (NINS), 650 North Aohoku Place, Hilo, HI 96720, USA

¹⁴ Metaspac, 36 Nonhyeon-ro, Gangnam-gu, Seoul 06312, Republic Of Korea

¹⁵ Department of Astronomical Science, SOKENDAI (The Graduate University for Advanced Studies), Osawa 2-21-1, Mitaka, Tokyo, 181-8588, Japan

¹⁶ Observatoire de Genève, Université de Genève, 51 Ch. des Maillettes, 1290 Versoix, Switzerland

¹⁷ NSF's National Optical-Infrared Astronomy Research Laboratory, 950 North Cherry Avenue, Tucson 85719, USA

¹⁸ Leiden Observatory, Leiden University, PO Box 9513, NL-2300 RA, Leiden, The Netherlands

¹⁹ Department of Physics, ETH Zürich, Wolfgang-Pauli-Strasse 27, 8093 Zürich, Switzerland

²⁰ Univ Lyon, Univ Lyon1, ENS de Lyon, CNRS, Centre de Recherche Astrophysique de Lyon UMR5574, F-69230 Saint-Genis-Laval, France

²¹ Research Center for Space and Cosmic Evolution, Ehime University, Matsuyama, Ehime 790-8577, Japan

²² Centre for Astrophysics & Supercomputing, Swinburne University of Technology, PO Box 218, Hawthorn, VIC 3112, Australia

²³ Department of Astronomy, Graduate School of Science, The University of Tokyo, 7-3-1 Hongo, Bunkyo, Tokyo 113-0033, Japan

Received 2021 August 9; revised 2021 October 26; accepted 2021 October 29; published 2022 January 31

Abstract

We present Keck/LRIS follow-up spectroscopy for 13 photometric candidates of extremely metal-poor galaxies (EMPGs) selected by a machine-learning technique applied to the deep (~ 26 AB mag) optical and wide-area (~ 500 deg²) Subaru imaging data in the EMPRESS survey. Nine out of the 13 candidates are EMPGs with an oxygen abundance (O/H) less than $\sim 10\%$ solar value (O/H)_⊙, and four sources are contaminants of moderately metal-rich galaxies or no emission-line objects. Notably, two out of the nine EMPGs have extremely low stellar masses and oxygen abundances of $5 \times 10^4\text{--}7 \times 10^5 M_\odot$ and 2%–3% (O/H)_⊙, respectively. With a sample of five EMPGs with (Fe/O) measurements, two (three) of which are taken from this study (the literature), we confirm that two EMPGs with the lowest (O/H) ratios of $\sim 2\%$ (O/H)_⊙ show high (Fe/O) ratios of ~ 0.1 , close to the solar abundance ratio. Comparing galaxy chemical enrichment models, we find that the two EMPGs cannot be explained by a scenario of metal-poor gas accretion/episodic star formation history due to their low (N/O) ratios. We conclude that the two EMPGs can be reproduced by the inclusion of bright hypernovae and/or hypothetical pair-instability supernovae (SNe) preferentially produced in a metal-poor environment. This conclusion implies that primordial galaxies at $z \sim 10$ could have a high abundance of Fe that did not originate from Type Ia SNe with delays and that Fe may not serve as a cosmic clock for primordial galaxies.


Unified Astronomy Thesaurus concepts: Galaxy formation (595); Galaxy structure (622); Star formation (1569); Galaxy chemical evolution (580); Dwarf galaxies (416)

1. Introduction

Galaxies in the early-formation phase are the keys to understanding galaxy formation and evolution. Young galaxies, especially galaxies with stellar ages below ~ 300 Myr, are

expected to be metal poor because low- and intermediate-mass stars cannot contribute to chemical enrichment before finishing lifetimes of ~ 300 Myr as main-sequence stars. Wise et al. (2012) predict that the first galaxy at $z \gtrsim 7$ (corresponding to the stellar age of $\lesssim 300$ Myr) has a halo mass of $10^7\text{--}10^9 M_\odot$, a stellar mass of $10^4\text{--}10^6 M_\odot$, and metallicity of 0.1%–1% solar abundance.

In such an extremely low-metallicity environment, progenitor gas clouds of stars are also metal poor. The metal-poor gas

 Original content from this work may be used under the terms of the [Creative Commons Attribution 4.0 licence](https://creativecommons.org/licenses/by/4.0/). Any further distribution of this work must maintain attribution to the author(s) and the title of the work, journal citation and DOI.

cools less efficiently than metal-rich gas because metals are much more efficient coolants than hydrogen. In such a metal-poor and high-temperature environment, protostellar cores exhibit large Jeans masses, consequently evolving into massive stars. Performing cosmological zoom-in simulations, Hirano et al. (2015) obtain $\sim 300 M_{\odot}$ stars in primordial star-forming clouds. Hirano et al. (2015) also report the mass distribution of first stars, which is indicative that very massive ($\gtrsim 100 M_{\odot}$) stars are born in a metal-free environment.

Metal-poor (and thus young) galaxies potentially undergo chemical evolutions largely affected by massive stars. Iron-to-oxygen (Fe/O) abundance ratios especially strongly depend on galaxy ages and initial mass functions (IMFs) because stars with different masses undergo different types of supernova (SN) explosions ejecting different amounts of iron and oxygen (Section 6.1). If we calculate ejecta from Type Ia SNe and core-collapse SNe (CCSNe) only, the Fe/O ratio monotonically increases with age (and thus can serve as a cosmic clock; Xing et al. 2019). Before the appearance of Type Ia SNe, however, high-Fe/O gas can also be produced by hypernovae (HNe) and pair-instability SNe (PISNe), whose progenitor stars are more massive than ~ 30 and $200 M_{\odot}$, respectively. Extremely young metal-poor galaxies may have high Fe/O ratios because both HNe and PISNe tend to be produced in metal-poor environments. Now we should evaluate the HN or PISN contributions to Fe/O in the early galaxy formation phase to test whether Fe/O can truly act as a cosmic clock in primordial galaxies.

We can verify whether HNe and/or PISNe play important roles in the Fe/O evolution of galaxies by observing extremely young ($\lesssim 10$ Myr) galaxies. However, such galaxies are intrinsically too faint because of their low stellar masses. Assuming $M_{*} = 10^6 M_{\odot}$ (Wise et al. 2012) and the large rest-frame equivalent width of $EW_0(\text{H}\alpha) = 3700 \text{ \AA}$ under the assumptions of age of 1 Myr, being metal free, and constant star formation (Inoue 2011), we derive the H α flux of extremely young low-mass galaxy at each redshift. As illustrated in Figure 1, the expected H α fluxes of the young low-mass galaxies (black) are >1 dex smaller than the limiting fluxes of the current-best instruments of Keck/LRIS and Keck/MOSFIRE within the redshift range of $z \gtrsim 0.5$. Even using the forthcoming Thirty Meter Telescope (TMT) and James Webb Space Telescope (JWST), we can detect the H α of the young low-mass galaxies only at $z \lesssim 2$. This means that it is difficult to detect young galaxies having $M_{*} \lesssim 10^6 M_{\odot}$ at $z \gtrsim 2$ even with the forthcoming large telescopes without gravitational lensing (e.g., Kikuchi et al. 2020).

Complementing these high- z galaxy observations, various studies have actively investigated local young dwarf galaxies (e.g., Berg et al. 2019). Although characteristics and formation processes of local young galaxies would be different from high- z galaxies (Isobe et al. 2021, hereafter Paper III), local young galaxies are useful not only for studying galaxies at the early-formation stage but also for understanding local young galaxies themselves as living fossils of forming galaxies in the universe today. Although such low-mass and metal-poor galaxies become rarer toward lower redshifts (Morales-Luis et al. 2011; Behroozi et al. 2013), recent studies show the presence of extremely metal-poor galaxies (EMPGs; defined as galaxies with $\leq 12 + \log(\text{O}/\text{H}) = 7.69 = 10\% (\text{O}/\text{H})_{\odot}$) in the local universe such as SBS 0335–052 (Izotov et al. 2009), AGC 198691 (Hirschauer et al. 2016), J1234+3901 (Izotov et al. 2019), Little Cub (Hsyu et al. 2017), DDO68 (Pustilnik et al. 2005), and IZw18 (Izotov & Thuan 1998). A blind H I survey

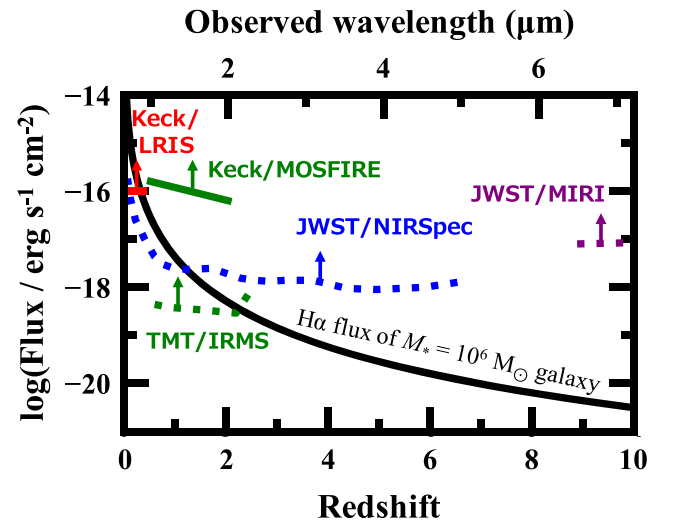


Figure 1. Expected H α flux of young galaxies with $M_{*} = 10^6 M_{\odot}$ and $EW_0(\text{H}\alpha) = 3700 \text{ \AA}$ at a given redshift (black solid curve). The red and green solid lines indicate the limiting fluxes of the current-best instruments of Keck/LRIS and Keck/MOSFIRE, respectively. The green, blue, and purple dotted lines represent the limiting fluxes of the near-future instruments of TMT/IRMS, JWST/NIRSpec, and JWST/MIRI, respectively. These limiting fluxes are calculated under the assumption that a point source has an emission line that should be detected at a signal-to-noise ratio of 10 in an exposure time of 10,000 s. The limiting fluxes of the instruments of TMT and JWST are derived from Hees et al. (2015) and Gardner et al. (2006), respectively.

(ALFALFA) has identified Leo P with $\sim 3\% (\text{O}/\text{H})_{\odot}$ (Skillman et al. 2013). Significant progress has been made recently with the EMPG spectroscopic and photometric samples from the Sloan Digital Sky Survey (SDSS). Sánchez Almeida et al. (2016) found 196 EMPGs from the SDSS spectroscopic data, and Izotov et al. (2018) identified J0811+4730 with a metallicity down to $2\% (\text{O}/\text{H})_{\odot}$. The SDSS imaging data have largely contributed to the identification of many EMPGs (e.g., James et al. 2015, 2017; Hsyu et al. 2018; Senchyna & Stark 2019).

However, such previous studies based on the SDSS are not ideal for pinpointing low-mass (and thus faint) EMPGs due to their shallow data. Kojima et al. (2020; hereafter Paper I) have launched a project entitled “Extremely Metal-Poor Representatives Explored by the Subaru Survey (EMPRESS)” with Subaru/Hyper Suprime-Cam (HSC) optical wide (500 deg^2) and deep (5σ limiting magnitude of $i_{\text{lim}} = 26$) images that are about 100 times deeper than those of SDSS (Aihara et al. 2019). EMPRESS has identified J1631+4426, whose metallicity is $1.6\% (\text{O}/\text{H})_{\odot}$. J1631+4426 has the lowest metallicity reported so far, with a low stellar mass of $\sim 10^6 M_{\odot}$.

While J1631+4426 (Paper I) and J0811+4730 (Izotov et al. 2018) have extremely low metallicities of $\sim 2\% (\text{O}/\text{H})_{\odot}$, Kojima et al. (2021; hereafter Paper II) reported that the two EMPGs show high Fe/O ratios of $\sim (\text{Fe}/\text{O})_{\odot}$. Paper II concludes that the two EMPGs are too young to be affected by the chemical enrichment of low- and intermediate-mass stars because the EMPGs have low N/O ratios. Alternatively, Paper II suggests that supermassive stars²⁴ may contribute to Fe/O

²⁴ More precisely, Paper II predicts supermassive stars beyond $300 M_{\odot}$. However, such massive stars are not likely to contribute to the Fe/O enhancements of EMPGs unless the stars rotate very fast (Shibata & Shapiro 2002).

enhancements, while the contribution has not been evaluated quantitatively.

This paper is the fourth paper of EMPRESS, reporting spectroscopic follow-up observations for the remaining EMPG candidates with Keck Telescope. We also derive chemical properties of the EMPGs including $12 + \log(\text{O}/\text{H})$ and Fe/O to discuss the chemical enrichment of galaxies in the early-formation phase. We present the EMPG sample in Section 2. In Section 3 we explain our optical spectroscopy and data reductions. We explain our data analysis in Section 4. We report and discuss the chemical properties of EMPGs in Section 5. We discuss further the origin of the Fe/O enhancements of the EMPGs in Section 6. Section 7 summarizes our findings. Throughout this paper, magnitudes are in the AB system (Oke & Gunn 1983), and we assume a standard ΛCDM cosmology with parameters of $(\Omega_m, \Omega_\Lambda, H_0) = (0.3, 0.7, 70 \text{ km s}^{-1} \text{ Mpc}^{-1})$. The definition of solar metallicity Z_\odot is given by $12 + \log(\text{O}/\text{H}) = 8.69$ (Asplund et al. 2021). Solar abundance ratios of $\log(\text{Ne}/\text{O})$, $\log(\text{Ar}/\text{O})$, $\log(\text{N}/\text{O})$, $\log(\text{Fe}/\text{O})$ are -0.63 , -2.31 , -0.86 , and -1.23 , respectively (Asplund et al. 2021).

2. Sample

We use a photometric sample of EMPG candidates selected in Paper I. The Paper I photometric sample consists of EMPG candidates identified from the data of HSC and SDSS, which we refer to as HSC EMPG candidates and SDSS EMPG candidates, respectively. In this paper, we do not use SDSS EMPG candidates, because the SDSS EMPG candidates include more contaminants than the HSC EMPG candidates (Paper I). The catalog of the HSC EMPG candidates is developed with the HSC-SSP S17A and S18A data (Aihara et al. 2019), which are wide and deep enough to search for rare and faint EMPGs. The HSC EMPG candidates are selected from ~ 46 million sources whose photometric measurements are brighter than 5σ limiting magnitudes in all of the four broad bands, $g < 26.5$, $r < 26.0$, $i < 25.8$, and $z < 25.2$ mag (Ono et al. 2018), which correspond to absolute magnitudes at $z = 0.03$ of $M_g < -9.1$, $M_r < -9.6$, $M_i < -9.8$, and $M_z < -10.4$ mag, respectively. The catalog consisting of these sources is referred to as the HSC source catalog.

With the HSC source catalog, Paper I isolates EMPGs from contaminants such as other types of galaxies, Galactic stars, and quasi-stellar objects (QSOs). Paper I aims to find galaxies at $z \leq 0.03$ with $\text{EW}_0(\text{H}\alpha) > 800 \text{ \AA}$ and $12 + \log(\text{O}/\text{H}) = 6.69\text{--}7.69$. Because it is difficult to distinguish EMPGs from the contaminants on two-color diagrams such as $r - i$ versus $g - r$, Paper I constructs a machine-learning classifier based on a deep neural network (DNN) with a training data set. The training data set is composed of mock photometric measurements for model spectra of EMPGs and the contaminants of other types of galaxies, Galactic stars, and QSOs. The DNN allows us to isolate EMPGs from the contaminants with nonlinear boundaries in the multidimensional color space. Paper I finally obtained 27 HSC EMPG candidates from the HSC source catalog. Paper I conducted spectroscopic follow-up observations with Magellan/LDSS-3, Magellan/MagE, Keck/DEIMOS, and Subaru/FOCAS for 4 out of the 27 HSC EMPG candidates and confirmed that all of the four HSC EMPG candidates are truly emission-line galaxies with the low metallicity of $12 + \log(\text{O}/\text{H}) = 6.90\text{--}8.27$ (i.e., $1.6\%\text{--}38\% Z_\odot$). Paper I finds that two out of the four HSC EMPG

Table 1
Coordinates of the HSC EMPG Candidates

#	ID	R.A.	Decl.
(1)	(2)	hh:mm:ss	dd:mm:ss
		(3)	(4)
1	J0156-0421	01:56:51.6	-04:21:25.2
2	J0159-0622	01:59:43.8	-06:22:32.8
3	J0210-0124	02:10:12.0	-01:24:51.1
4	J0214-0243	02:14:24.3	-02:43:54.4
5	J0226-0517	02:26:57.6	-05:17:47.3
6	J0232-0248	02:32:13.3	-02:48:19.3
7	J1608+4337	16:08:11.0	+43:37:53.4
8	J2236+0444	22:36:12.4	+04:44:22.3
9	J2321+0125	23:21:52.2	+01:25:55.0
10	J2355+0200	23:55:30.1	+02:00:16.0
11	J0228-0256	02:28:36.3	-02:56:45.7
12	J2221-0015	22:21:26.1	-00:15:49.5
13	J2319+0136	23:19:33.6	+01:36:50.2

Note. (1) Number. (2) ID. (3) Right ascension in J2000. (4) decl. in J2000.

candidates meet the EMPG criterion of $12 + \log(\text{O}/\text{H}) < 7.69$ (i.e., $< 10\% Z_\odot$). We refer to the two EMPGs as HSC spectroscopic EMPGs. There remain 23 ($= 27 - 4$) HSC EMPG candidates that are not spectroscopically confirmed in Paper I. We refer to the 23 candidates as HSC photometric EMPGs.

3. Observations and Data Reduction

3.1. Spectroscopic Follow-up Observations with Keck/LRIS

In this paper, we report spectroscopic observations with the Low Resolution Imaging Spectrograph (LRIS; Oke et al. 1995). LRIS is an imaging spectrometer installed at the Cassegrain focus of the Keck Telescope, whose aperture area is equivalent to that with a circular aperture of 9.96 m in diameter. LRIS has both blue and red channels that roughly cover wavelength ranges of 3000–6000 and 6000–10000 \AA , respectively. LRIS can perform long-slit spectroscopy or multiobject spectroscopy (MOS).

We conducted spectroscopy with Keck/LRIS (PI: T. Kojima) for 13 out of the 23 HSC photometric EMPGs. The 13 targets were all HSC photometric EMPGs observable on the observing night of 2019 August 31. Coordinates of the 13 HSC photometric EMPGs are listed in Table 1. We utilized the MOS mode and long-slit mode for seven and six candidates, respectively. The slit widths were $1''.5$ for all targets. We used the 600 lines mm^{-1} grism blazed at 4000 \AA on the blue channel and the 600 lines mm^{-1} grating blazed at 7500 \AA on the red channel. The LRIS spectroscopy of the blue and red channels covered the wavelength ranges of $\lambda \sim 3000\text{--}5500$ and 6000–9000 \AA with the spectral resolutions of ~ 4 and 5 \AA in FWHM, respectively. We also observed standard stars of DOP type, Feige 110 (R.A. = 23:19:58.4, Decl. = -05:09:56 in J2000); B2III type, BD+40 4032 (RA = 20:06:40.0, Dec. = +41:06:15 in J2000); and B6V type, Feige 25 (R.A. = 02:36:00.0, Decl. = +05:15:17 in J2000). The sky was clear during the observations with seeing sizes of $0''.8$. The observations are summarized in Table 2.

Figure 2 shows HSC images of the 13 HSC photometric EMPGs that we observed with LRIS. We note that many of the HSC photometric EMPGs (#2, 3, 4, 5, 6, 7, 9, 10, 11, and 13 in Figure 2) have diffuse structures (EMPG-tails; Paper III).

Table 2
Summary of the LRIS Observations

#	ID	Mode	Exposure sec
(1)	(2)	(3)	(4)
1	J0156–0421	Long slit	1200
2	J0159–0622	Long slit	1200
3	J0210–0124	MOS	1200
4	J0214–0243	MOS	1200
5	J0226–0517	MOS	1200
6	J0232–0248	MOS	1200
7	J1608+4337	MOS	1800
8	J2236+0444	Long slit	2400
9	J2321+0125	Long slit	3600
10	J2355+0200	MOS	2400
11 ^a	J0228–0256	Long slit	1200
12 ^b	J2221–0015	Long slit	2400
13 ^b	J2319+0136	Long slit	600

Notes. (1) Number. (2) ID. (3) Observing mode (Section 3.1). (4) Exposure time.

^a Contaminant: metal-rich galaxy (see Section 3.2)

^b Contaminant: no emission line (see Section 3.2)

We discuss the contribution of the EMPG-tails to the flux measurement of the HSC photometric EMPGs in Section 4.1.

3.2. Data Reduction

To reduce and calibrate the data taken with LRIS, we use the IRAF package. The reduction and calibration processes include bias subtraction, flat-fielding, cosmic-ray cleaning, sky subtraction, wavelength calibration, one-dimensional (1D) spectrum extraction, flux calibration, atmospheric-absorption correction, and Galactic-reddening correction. The 1D spectra are derived from apertures centered on the blue compact component of the HSC photometric EMPGs. We use the standard star Feige 110 for the flux calibration. The wavelengths are calibrated with the HgNeArCdZnKrXe lamp. We correct the atmospheric absorption with the extinction curve at Maunakea Observatories (Béland et al. 1988). The Galactic-reddening value for each target is drawn from the NASA/IPAC Infrared Science Archive (IRSA)²⁵ based on the Schlafly & Finkbeiner (2011) estimates.

We detect emission lines from 11 out of the 13 HSC photometric EMPGs. The remaining two HSC photometric EMPGs (J2221–0015 and J2319+0136; #12 and 13) with no emission lines detected are probably contaminants because the $H\alpha$ fluxes estimated from r -band excesses are $4 \times 10^{-15} - 1 \times 10^{-14} \text{ erg s}^{-1} \text{ cm}^{-2}$, which should be detectable with the 10 minute exposure of LRIS. Figures 3 and 4 present the reduced spectra of the 11 HSC photometric EMPGs. One out of the 11 HSC photometric EMPGs (J0228–0256; #11 in Figure 4) is located at $z=0.21$, which is out of the redshift range where Paper I aims to select EMPGs (Section 2). Because #11 shows a high $[\text{O II}]\lambda\lambda 3727, 3729/[\text{O III}]\lambda 5007$ ratio and a strong Balmer break, #11 is likely to be a metal-rich galaxy. The remaining 10 HSC photometric EMPGs appear to be located at the redshifts of $z=0.009-0.056$, where Paper I aims to select EMPGs. Hereafter we refer to these 10 HSC photometric EMPGs as LRIS EMPG candidates. The inset panels of Figures 3 and 4 indicate that many of the LRIS

EMPG candidates have emission lines with blue wings, suggestive of the outflow (Xu et al. 2021; cf. Section 5.2).

4. Analysis

4.1. Flux Measurement

We measure central wavelengths, emission-line fluxes, and continua of the LRIS EMPG candidates (Section 3.2) with best-fit Gaussian (+constant) profiles using the `scipy.optimize` package. We also estimate flux errors containing read-out noise and photon noise of sky and object emissions. None of the LRIS EMPG candidates show broad Balmer lines or high-ionization lines such as $[\text{Fe VII}]\lambda 6087$, which suggests that the radiation from active galactic nuclei (AGNs) is not dominant in any LRIS EMPG candidate. We detect faint $[\text{O III}]\lambda 4363$ lines from all 10 LRIS EMPG candidates. Because none of the LRIS EMPG candidates show $[\text{Fe II}]\lambda 4288$, whose flux is larger than that of $[\text{Fe II}]\lambda 4359$ ²⁶, the contamination of $[\text{O III}]\lambda 4363$ from $[\text{Fe II}]\lambda 4359$ is negligible. We also obtain very faint $[\text{Fe III}]\lambda 4658$ lines from 2 out of the 10 LRIS EMPG candidates (#2 and 7), which enable us to calculate Fe/O abundance ratios. This flux measurement probably represents an average of the whole galaxy because the size of a typical HSC EMPG is $\sim 0''.3$ ($\sim 200 \text{ pc}$; Paper III), which is smaller than the seeing size of $0''.8$ and the slit width of $1''.5$. Redshifts are derived from the ratios between the observed central wavelengths and the rest-frame wavelengths in the air of $H\beta$ lines.

Color excesses $E(B-V)$ are derived from the Balmer decrement under the assumptions of the dust attenuation curve of Calzetti et al. (2000)²⁷ and the case B recombination. We calculate $E(B-V)$, electron temperature T_e , and electron density n_e iteratively so that all these properties are consistent with each other (see also Section 4.2). We obtain intrinsic values of Balmer emission-line ratios using PyNeb (Luridiana et al. 2015; v1.1.15) with a transition probability of hydrogen listed in Table 3. We derive the χ^2 of $E(B-V)$ from each Balmer emission-line ratio containing $H\alpha$, $H\beta$, $H\gamma$, and $H\delta$. Then, we find the best $E(B-V)$ values, which give the least χ^2 . We also obtain $\pm 68\%$ confidence intervals of $E(B-V)$ based on χ^2 . From all LRIS EMPG candidates, we detect $H\gamma$ and $H\delta$ lines with signal-to-noise ratio (S/N) > 13 and $S/N > 5$, respectively. We also confirm that none of the $H\delta$, $H\gamma$, $H\beta$, and $H\alpha$ lines show significant stellar absorption. Using the $E(B-V)$ and the Calzetti et al. (2000) attenuation curve, we derive dust-corrected fluxes. We note that the dust-corrected fluxes are not very different from the observed ones, because most of the LRIS EMPG candidates show $E(B-V) \sim 0$ (i.e., dust poor). The dust-corrected fluxes are summarized in Table 4. Again, we note that we detect the weak $[\text{Fe III}]\lambda 4658$ lines from 2 out of the 10 LRIS EMPG candidates, which are used to derive the Fe abundance. Other fundamental properties such as the redshift, rest-frame equivalent width of $\text{EW}_0(H\beta)$, and $E(B-V)$ are listed in Table 5. Checking 2D spectra, we find that emission lines of EMPG-tails can contaminate those of EMPGs by at most 10%. We then add the uncertainties to lower errors of fluxes of EMPGs with EMPG-tails. On the other hand, stellar continua

²⁶ PyNeb provides $[\text{Fe II}]\lambda 4359 = 0.73 \times [\text{Fe II}]\lambda 4288$ under the assumptions of $T_e = 20,000 \text{ K}$ and $n_e = 100 \text{ cm}^{-3}$.

²⁷ A choice of attenuation curves does not change our results significantly because the Balmer decrements of the LRIS EMPG candidates are comparable to those under the assumption of the case B recombination (i.e., dust poor).

²⁵ <https://irsa.ipac.caltech.edu/applications/DUST/>

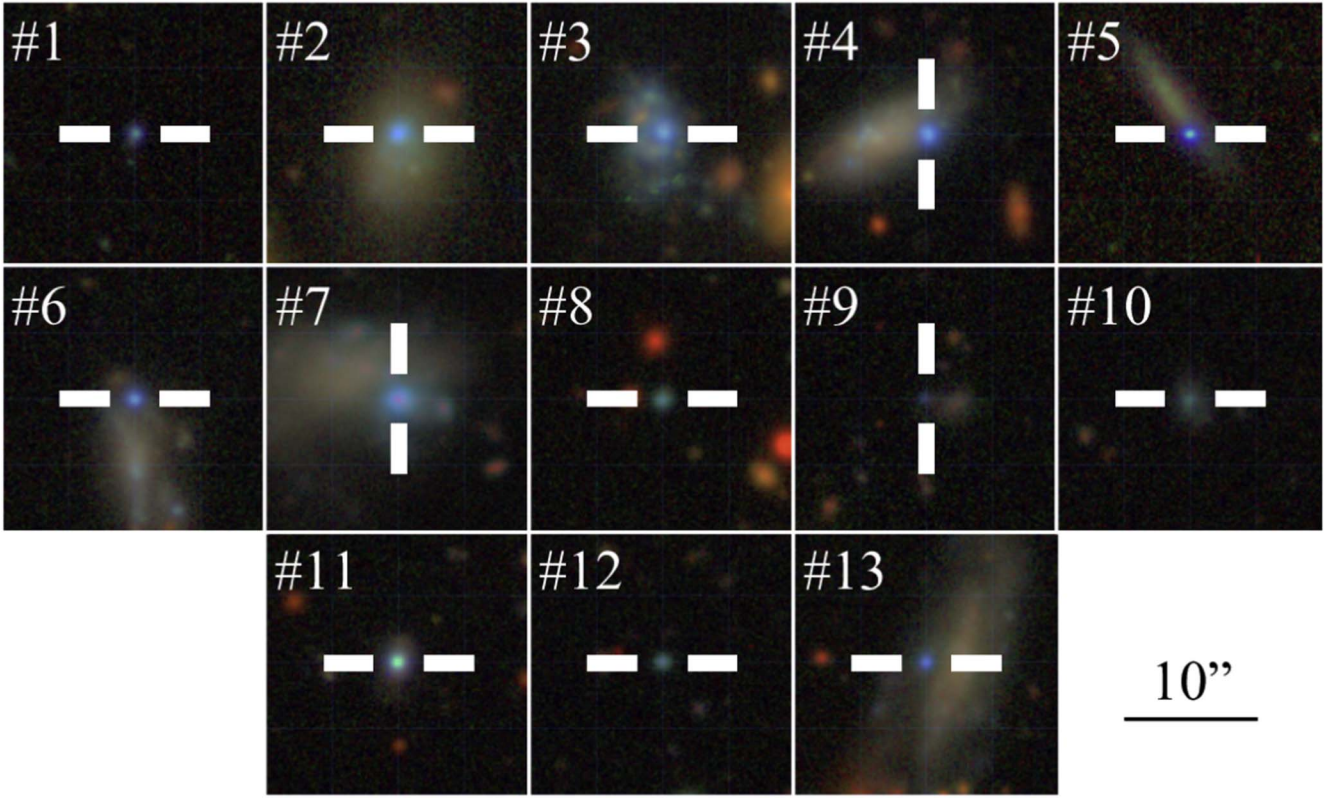


Figure 2. HSC *gri*-composite images of the 13 HSC photometric EMPGs that we observed with LRIS. The HSC *g*, *r*, and *i* bands correspond to the blue, green, and red colors in the figure, respectively. Each EMPG is located between the two white bars of each panel. The cutout size is $20'' \times 20''$. The number shown at the top-left corner of each panel corresponds to the number in Table 2.

of EMPG-tails potentially contaminate those of EMPGs by at most 50%, which implies that the $EW_0(H\beta)$ of EMPGs would be underestimated. We calculate errors of $EW_0(H\beta)$ including the uncertainties of stellar continua as well as those of $H\beta$ fluxes.

4.2. Chemical Property

All of the LRIS EMPG candidates have $[O\text{ III}]\lambda 4363$ detections, which allows us to derive metallicities and other element abundances with the direct- T_e method (e.g., Izotov 2006) as described below.

The electron temperature T_e is calculated from two collisional excitation lines of the same ion such as O^{2+} , because the collisional excitation rate is determined by T_e . Using the PyNeb package `getCrossTemDen` with the latest atomic data and temperature relationship listed in Table 3, we derive the T_e of O^{2+} ($T_e(O\text{ III})$) and n_e from emission-line ratios of $[O\text{ III}]\lambda 4363/[O\text{ III}]\lambda\lambda 4959,5007$ and $[S\text{ II}]\lambda 6731/[S\text{ II}]\lambda 6716$, respectively. If $[S\text{ II}]\lambda 6716$ is not available, we calculate T_e with a fixed n_e of 100 cm^{-3} , which is roughly consistent with that of EMPGs (e.g., Paper I). We summarize results of T_e and n_e in Table 5. Again, our iterative calculations provide self-consistent values of $E(B-V)$, $T_e(O\text{ III})$, and n_e (cf. Section 4.1). We also note that T_e is mainly determined by the ratio $F([O\text{ III}]\lambda 4363)/F([O\text{ III}]\lambda\lambda 4959, 5007)$ and almost independent of n_e because the derived n_e values are much lower than a critical density of $6.4 \times 10^5\text{ cm}^{-3}$ for the $[O\text{ III}]\lambda 4363$ transition of $^1S_0 \rightarrow ^1D_2$.

Using PyNeb with the latest atomic data and temperature relationships listed in Table 3, we derive ion abundance ratios of O^+/H^+ and O^{2+}/H^+ from emission-line ratios of $[O\text{ II}]\lambda\lambda$

$3727,3729/H\beta$ and $[O\text{ III}]\lambda\lambda 4959,5007/H\beta$ with electron temperatures of $T_e(O\text{ II})$ and $T_e(O\text{ III})$, respectively, and the derived n_e . We calculate $T_e(O\text{ II})$ using an empirical relation of

$$T_e(O\text{ II}) = 0.7T_e(O\text{ III}) + 3000 \quad (1)$$

(Garnett 1992). Just adding O^+/H^+ to O^{2+}/H^+ , we finally obtain $12 + \log(O/H)$. We note that neutral oxygen is negligible in H II regions because the ionization potential of neutral oxygen atoms is 13.6 eV, the same as that of neutral hydrogen atoms. We also ignore O^{3+} and higher-order oxygen ions for consistency with previous works (e.g., Izotov 2006; Paper I)²⁸.

Using the latest atomic data and temperature relationships listed in Table 3, we can also derive other gas-phase ion abundances such as Ne^{2+}/H^+ , Ar^{2+}/H^+ , N^+/H^+ , and Fe^{2+}/H^+ with optical emission lines of $[Ne\text{ III}]\lambda 3869$, $[Ar\text{ III}]\lambda 7136$, $[N\text{ II}]\lambda\lambda 6548,6584$, and $[Fe\text{ III}]\lambda 4658$, respectively. We use $T_e(O\text{ III})$ and $T_e(S\text{ III})$ to calculate high- and intermediate-ionization ion abundances of Ne^{2+} and Ar^{2+} , respectively. We derive $T_e(S\text{ III})$ from an empirical relation of

$$T_e(S\text{ III}) = 0.83 \times T_e(O\text{ III}) + 1700 \quad (2)$$

(Garnett 1992). We adopt $T_e(O\text{ II})$ to estimate low-ionization ion abundances of N^+ and Fe^{2+} .

²⁸ O^{3+} and higher-order oxygen ions are usually ignored because they have ionization potentials of $>55\text{ eV}$, which cannot be generated by the UV radiation of typical stars. However, supermassive or metal-free stars can efficiently produce high-energy photons above 55 eV (Vink 2018 and Tumlinson & Shull 2000, respectively). If such stars exist in EMPGs (e.g., Paper II), the higher-order oxygen ions may not be negligible.

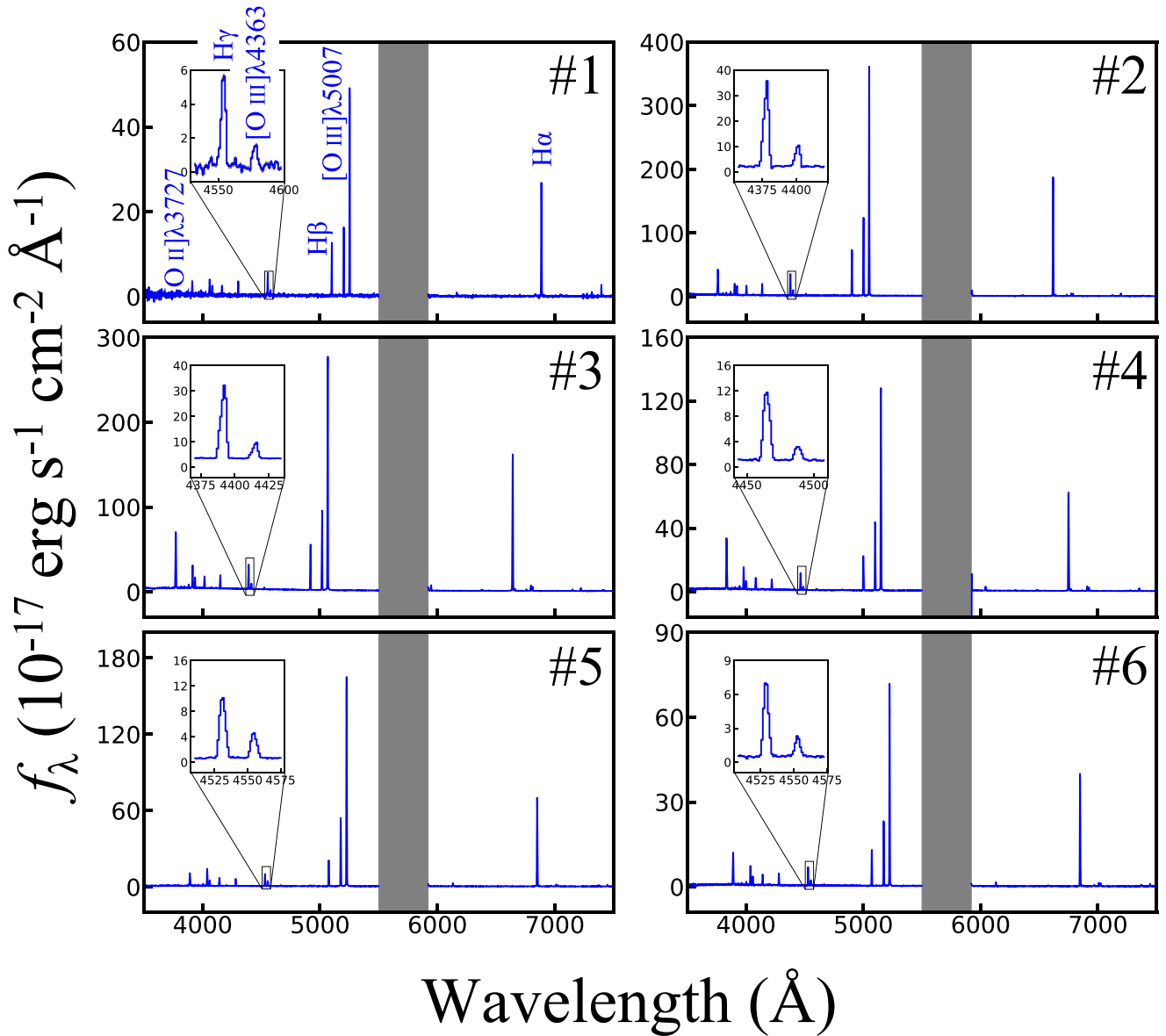


Figure 3. Reduced spectra of 6 out of the 11 HSC photometric EMPGs. The gray shaded regions indicate the gaps between the LRIS blue and red channels. The number shown at the top-right corner of each panel corresponds to the number in Table 4. The inset panel at the top-left corner of each panel illustrates an enlarged view of the spectrum around H γ and [O III] λ 4363. The gray lines indicate the errors of the spectra.

Table 3
Atomic Data

Ion (1)	Emission Process (2)	Transition Probability (3)	Collision Strength (4)
H ⁰	Re	Storey & Hummer (1995)	...
O ⁺	CE	Froese Fischer & Tachiev (2004)	Kisielius et al. (2009)
O ²⁺	CE	Froese Fischer & Tachiev (2004)	Storey et al. (2014)
Ne ²⁺	CE	Froese Fischer & Tachiev (2004)	McLaughlin & Bell (2000)
Ar ²⁺	CE	Munoz Burgos et al. (2009)	Munoz Burgos et al. (2009)
N ⁺	CE	Froese Fischer & Tachiev (2004)	Tayal (2011)
Fe ²⁺	CE	Quinet (1996); Johansson et al. (2000)	Zhang (1996)

Note. (1) Ion. (2) Emission process. Re and CE represent recombination and collisional excitations, respectively. (3) Reference of the transition probability of each ion. (4) Reference of the collision strength of each ion. We note that these atomic data and temperature relationships are the latest ones applied in Berg et al. (2015) and Paper II.

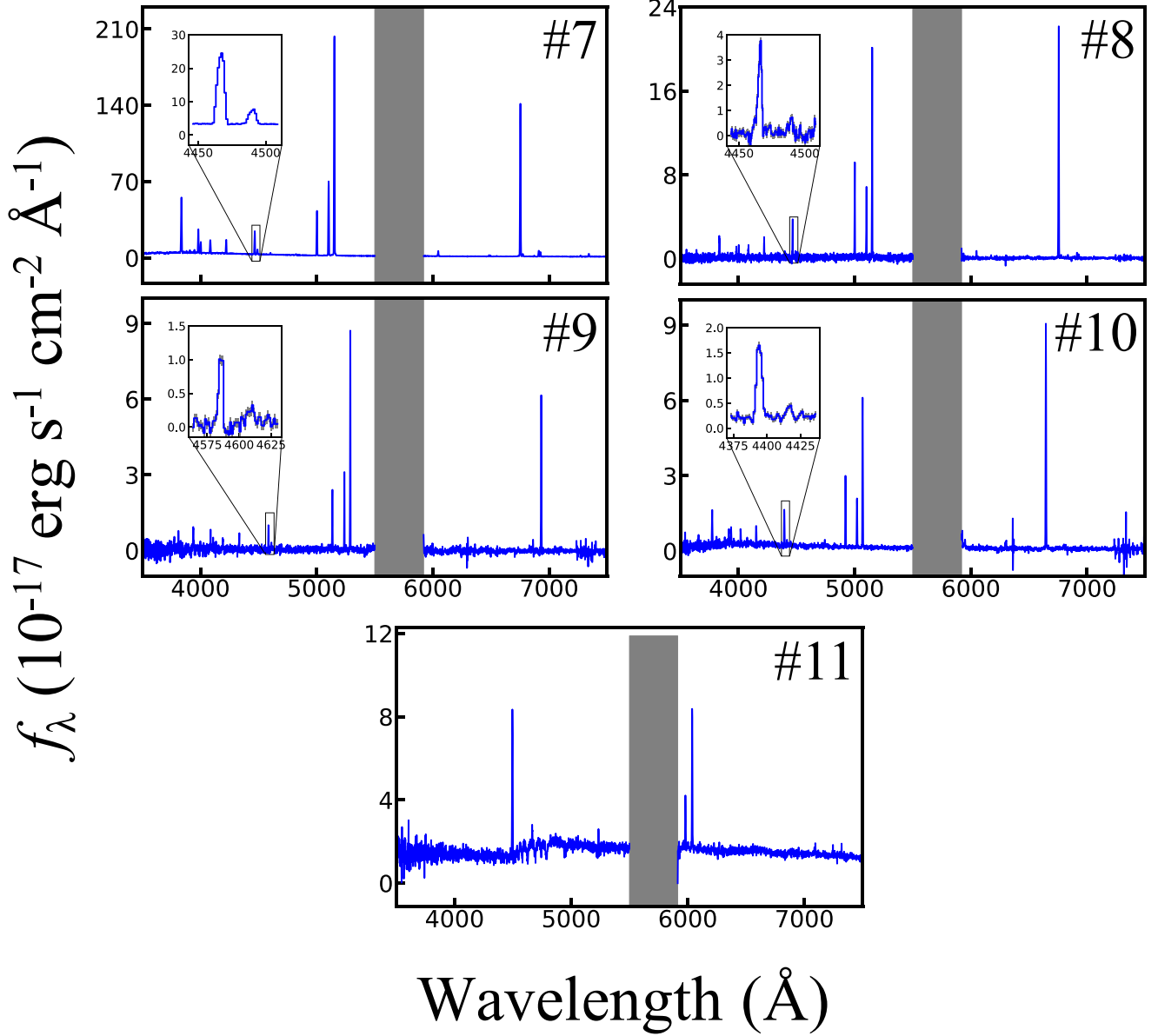


Figure 4. Reduced spectra of the remaining 5 of the 11 HSC photometric EMPGs. The symbols are the same as those in Figure 3. J0228–0256 (#11) is a metal-rich galaxy at $z = 0.21$ (Section 3.2). The other 10 HSC photometric EMPGs are EMPG candidates at $z = 0.009\text{--}0.056$.

Using the ionization correction factor (ICF) of Izotov (2006), which can be described by O^+ and O^{2+} ions, we derive a total gas-phase abundance for each element from each ion abundance. In the case of iron, for example, the abundance ratio Fe/H is calculated by

$$\frac{\text{Fe}}{\text{H}} = \frac{\text{Fe}^{2+}}{\text{H}^+} \times \text{ICF}(\text{Fe}^{2+}). \quad (3)$$

It should be noted that the ICFs slightly depend on the metallicity as follows:

$$\begin{aligned} \text{ICF}(\text{Fe}^{2+}) &= 0.158\nu + 0.958 + 0.004/\nu, \text{ lowZ} \\ &= 0.104\nu + 0.980 + 0.001/\nu, \text{ intermed.Z} \\ &= 0.238\nu + 0.931 + 0.004/\nu, \text{ highZ}, \end{aligned} \quad (4)$$

where $\nu = \text{O}^+ / (\text{O}^+ + \text{O}^{2+})$. We adopt low-, intermediate-, and high-metallicity ICFs for galaxies with $12 + \log(\text{O}/\text{H}) \leq 7.2$,

$7.2 < 12 + \log(\text{O}/\text{H}) < 8.2$, and $12 + \log(\text{O}/\text{H}) \geq 8.2$, respectively (Izotov 2006). We also estimate iron abundances using the ICF of Rodriguez & Rubin (2005), which incorporates Fe^{3+} abundances. We confirm that Fe/O ratios based on Rodriguez & Rubin (2005) are ~ 0.2 dex lower than those of Izotov (2006) as discussed in Paper II. We add the offsets to lower errors of Fe/O .

In order to estimate the errors of the gas-phase element abundance ratios, we randomly fluctuate flux values based on the flux errors. We calculate the abundance ratios 1000 times and then obtain median values with $\pm 68\%$ confidence intervals of the abundance ratios. We note that our LRIS deep spectroscopy provides high S/Ns of $[\text{O III}]\lambda 4363$ especially for LRIS EMPG candidates #1–7, which result in small errors of $12 + \log(\text{O}/\text{H})$.

We summarize the results in Table 6. Because all of the LRIS EMPG candidates are dust poor (Section 4.1), the gas-

Table 4
Dust-corrected Fluxes of the LRIS EMPG Candidates

# (1)	ID (2)	[O II] $\lambda\lambda$ 3727,3729 (3)	[Ne III] λ 3869 (4)	H δ (5)	[Fe II] λ 4288 (6)	H γ (7)	[O III] λ 4363 (8)	[Fe III] λ 4658 (9)
1	J0156–0421	38.6 \pm 1.5	31.4 \pm 1.4	25.1 \pm 1.1	<4.4	45.8 \pm 1.8	11.0 \pm 1.2	<5.3
2	J0159–0622	78.6 \pm 0.5	29.6 \pm 0.3	26.6 \pm 0.2	<0.7	47.2 \pm 0.4	11.6 \pm 0.2	0.8 \pm 0.4
3	J0210–0124	169.5 \pm 0.6	50.2 \pm 0.3	31.0 \pm 0.3	<0.6	53.4 \pm 0.6	11.1 \pm 0.3	<1.1
4	J0214–0243	170.4 \pm 0.7	61.6 \pm 0.5	30.2 \pm 0.5	<1.4	51.5 \pm 0.7	10.1 \pm 0.5	<1.8
5	J0226–0517	66.0 \pm 0.6	75.1 \pm 0.6	30.2 \pm 0.5	<1.6	50.8 \pm 0.8	21.0 \pm 0.6	<1.6
6	J0232–0248	127.9 \pm 1.0	53.4 \pm 0.6	31.5 \pm 0.7	<2.2	52.7 \pm 1.2	13.5 \pm 0.7	<2.8
7	J1608+4337	148.9 \pm 0.5	53.3 \pm 0.3	31.5 \pm 0.3	<0.7	54.2 \pm 0.5	11.0 \pm 0.4	1.4 \pm 0.5
8	J2236+0444	49.3 \pm 3.8	16.3 \pm 2.3	30.4 \pm 2.3	<5.5	41.0 \pm 2.0	7.8 \pm 2.3	<5.8
9	J2321+0125	58.4 \pm 5.1	28.6 \pm 3.1	23.5 \pm 3.1	<14.5	50.3 \pm 4.0	14.5 \pm 6.3	<16.9
10	J2355+0200	62.8 \pm 1.8	17.1 \pm 1.4	28.7 \pm 1.6	<6.6	52.9 \pm 2.2	7.3 \pm 2.1	<7.4
# (1)	He II λ 4686 (10)	[Ar IV] λ 4711 (11)	[Ar IV] λ 4740 (12)	H β (13)	[O III] λ 4959 (14)	[O III] λ 5007 (15)	[C IV] λ 5808 (16)	He I λ 5876 (17)
1	<5.4	<4.2	<5.7	100.0 \pm 3.1	133.7 \pm 2.9	394.9 \pm 4.6	<2.4	8.9 \pm 0.8
2	<0.9	<1.9 \pm 0.2	1.3 \pm 0.3	100.0 \pm 0.7	156.8 \pm 0.9	485.1 \pm 1.6	...	14.0 \pm 0.2
3	<1.1	1.0 \pm 0.3	0.6 \pm 0.3	100.0 \pm 1.3	159.6 \pm 1.3	477.6 \pm 2.4	...	12.2 \pm 0.2
4	1.2 \pm 0.4	1.4 \pm 0.5	<1.5	100.0 \pm 1.3	194.7 \pm 2.0	573.0 \pm 3.4	<0.7	11.6 \pm 0.3
5	<1.6	4.3 \pm 0.6	3.2 \pm 0.6	100.0 \pm 1.2	259.0 \pm 2.6	765.7 \pm 3.5	<0.8	11.0 \pm 0.2
6	<2.8	<2.9	<3.0	100.0 \pm 2.3	180.9 \pm 3.1	539.9 \pm 4.2	<1.5	12.3 \pm 0.6
7	2.3 \pm 0.4	0.9 \pm 0.3	<1.0	100.0 \pm 1.1	162.0 \pm 1.5	476.6 \pm 2.5	<0.3	11.1 \pm 0.1
8	<7.4	<6.9	<6.1	100.0 \pm 2.4	68.1 \pm 2.4	196.2 \pm 3.4	<2.1	7.6 \pm 0.7
9	<18.0	<17.5	<13.4	100.0 \pm 7.5	127.8 \pm 6.6	362.7 \pm 8.4	<8.5	5.2 \pm 2.3
10	7.3 \pm 2.6	<10.0	<7.7	100.0 \pm 5.1	70.5 \pm 5.1	205.9 \pm 5.5	...	9.8 \pm 1.0
# (1)	[O I] λ 6300 (18)	[S III] λ 6312 (19)	[N II] λ 6548 (20)	H α (21)	[N II] λ 6584 (22)	He I λ 6678 (23)	[S II] λ 6716 (24)	[S II] λ 6731 (25)
1	3.4 \pm 1.2	2.3 \pm 1.0	<2.7	264.2 \pm 1.9	2.5 \pm 0.5	3.1 \pm 0.9	4.3 \pm 0.7	3.2 \pm 0.6
2	1.6 \pm 0.1	1.9 \pm 0.1	1.0 \pm 0.1	279.1 \pm 0.6	3.3 \pm 0.1	2.9 \pm 0.1	6.2 \pm 0.2	6.0 \pm 0.2
3	2.9 \pm 0.1	1.6 \pm 0.1	1.6 \pm 0.1	322.3 \pm 0.7	3.1 \pm 0.1	3.1 \pm 0.1	14.2 \pm 0.2	10.0 \pm 0.2
4	3.9 \pm 0.3	2.3 \pm 0.3	2.3 \pm 0.2	313.4 \pm 1.1	6.2 \pm 0.3	2.0 \pm 0.3	14.6 \pm 0.4	10.6 \pm 0.4
5	1.5 \pm 0.3	1.6 \pm 0.2	1.5 \pm 0.3	306.9 \pm 1.4	1.5 \pm 0.3	3.4 \pm 0.4	5.9 \pm 0.3	4.7 \pm 0.3
6	2.1 \pm 0.4	1.5 \pm 0.4	<1.7	322.0 \pm 2.0	2.2 \pm 0.5	3.3 \pm 0.5	9.8 \pm 0.5	7.2 \pm 0.5
7	2.9 \pm 0.1	1.9 \pm 0.1	2.0 \pm 0.1	325.8 \pm 0.7	5.3 \pm 0.2	1.7 \pm 0.1	13.4 \pm 0.2	10.3 \pm 0.2
8	2.2 \pm 0.8	<2.4	<2.6	261.2 \pm 1.3	<2.5	<3.3	5.7 \pm 0.7	5.1 \pm 1.2
9	<6.7	<7.1	<8.7	273.5 \pm 3.8	<10.4	<7.9	<7.8	5.3 \pm 2.6
10	2.9 \pm 0.7	<3.0	<3.1	302.1 \pm 2.1	<4.2	4.0 \pm 1.5	5.1 \pm 1.1	4.0 \pm 1.5
# (1)	He I λ 7065 (26)	[Ar III] λ 7136 (27)	[O II] λ 7320 (28)	[O II] λ 7330 (29)	$F(\text{H}\beta)$ 10^{-17} erg s $^{-1}$ cm $^{-2}$ (30)			
1	1.5 \pm 0.6	2.9 \pm 1.4	<2.7	<2.1	52.8 \pm 1.6			
2	2.4 \pm 0.1	5.7 \pm 0.2	1.1 \pm 0.1	1.1 \pm 0.2	519.5 \pm 3.6			
3	2.6 \pm 0.2	6.4 \pm 0.2	2.6 \pm 0.2	2.2 \pm 0.2	362.4 \pm 4.7			
4	<0.8	<1.1	<0.6	<0.6	152.4 \pm 2.0			
5	4.4 \pm 0.4	5.7 \pm 0.3	<0.5	0.9 \pm 0.4	209.0 \pm 2.5			
6	4.8 \pm 0.9	5.4 \pm 0.5	<1.3	1.9 \pm 0.7	92.9 \pm 2.1			
7	2.8 \pm 0.2	6.5 \pm 0.2	2.0 \pm 0.2	1.6 \pm 0.2	375.5 \pm 4.1			
8	1.5 \pm 0.6	<4.7	<2.8	<1.8	109.4 \pm 2.6			
9	<13.6	<12.1	<6.6	<6.1	12.6 \pm 0.9			
10	2.5 \pm 0.8	<5.2	5.8 \pm 1.8	<4.0	22.9 \pm 1.2			

Note. (1) Number. (2) ID. (3)–(29) Dust-corrected flux normalized by the H β flux. The upper limits represent S/N = 3 levels. The symbols “—” indicate the lack of data because the emission lines fall into the wavelength gap between the LRIS blue and red channels. (30) Aperture-corrected flux of H β . Note that the errors shown in this table include only statistical errors. The LRIS EMPG candidates with EMPG-tails (#2, 3, 4, 5, 6, 7, 9, and 10; Section 3.1) have fluxes with additional systematic lower errors (10% of the fluxes) that originated from the potential contaminations from the EMPG-tails (Section 4.1).

Table 5
Fundamental Properties of the LRIS EMPG Candidates

#	ID	Redshift	$12 + \log(\text{O}/\text{H})$	$\text{EW}_0(\text{H}\beta)$ Å	$E(B - V)$ mag	T_e 10^4 K	n_e cm^{-3}
(1)	(2)	(3)	(4)	(5)	(6)	(7)	(8)
1	J0156–0421	0.04907	$7.48^{+0.07}_{-0.06}$	>76.0	$0.00^{+0.04}_{-0.00}$	$1.79^{+0.12}_{-0.11}$	127^{+539}_{-127}
2	J0159–0622	0.00852	$7.68^{+0.04}_{-0.03}$	$127.0^{+19.8+63.5}_{-19.8-12.7}$	0.10 ± 0.01	$1.65^{+0.04}_{-0.04}$	735^{+196}_{-179}
3	J0210–0124	0.01172	$7.76^{+0.03}_{-0.03}$	$78.9^{+4.6+39.5}_{-4.6-7.9}$	0.06 ± 0.01	$1.62^{+0.04}_{-0.05}$	4^{+63}_{-4}
4	J0214–0243	0.02860	$7.96^{+0.04}_{-0.04}$	$106.5^{+8.2+53.3}_{-8.2-10.7}$	0.03 ± 0.01	$1.43^{+0.05}_{-0.04}$	64^{+96}_{-64}
5	J0226–0517	0.04386	$7.78^{+0.04}_{-0.04}$	$136.6^{+12.5+68.3}_{-12.5-13.7}$	0.14 ± 0.02	$1.78^{+0.05}_{-0.05}$	268^{+223}_{-177}
6	J0232–0248	0.04336	$7.73^{+0.04}_{-0.04}$	$109.0^{+18.1+54.5}_{-18.1-10.9}$	0.08 ± 0.02	$1.69^{+0.06}_{-0.06}$	76^{+192}_{-76}
7	J1608+4337	0.02896	$7.75^{+0.04}_{-0.04}$	$83.4^{+2.3+41.7}_{-2.3-8.3}$	0.08 ± 0.01	$1.62^{+0.05}_{-0.05}$	155^{+107}_{-78}
8	J2236+0444	0.02870	$7.05^{+0.17}_{-0.12}$	>44.8	0.28 ± 0.05	$2.22^{+0.30}_{-0.32}$	548^{+902}_{-516}
9	J2321+0125	0.05639	$7.28^{+0.29}_{-0.16}$	>39.6	$0.05^{+0.09}_{-0.05}$	$2.23^{+0.39}_{-0.48}$...
10	J2355+0200	0.01231	$7.15^{+0.20}_{-0.13}$	$78.0^{+20.5+39.0}_{-20.5-7.8}$	0.09 ± 0.05	$2.06^{+0.31}_{-0.35}$	214^{+1934}_{-214}

Note. (1) Number. (2) ID. (3) Redshift of $\text{H}\beta$, whose typical uncertainty is $\mathcal{O}(10^{-6})$. (4) $12 + \log(\text{O}/\text{H})$ in the gas phase. (5) Rest-frame equivalent width of $\text{H}\beta$. The lower limits indicate fluxes of $\text{H}\beta$ divided by continua of $S/N = 3$ levels. The first and second terms of the errors represent statistical and systematic errors, respectively. The systematic errors of the upper and lower errors correspond to the uncertainties originating from potential contaminations of stellar continua and $\text{H}\beta$ fluxes from EMPG-tails, respectively (Section 4.1). (6) $E(B - V)$. (7) Electron temperature T_e . (8) Electron density n_e . Note that LRIS EMPG #9 does not have an n_e measurement because $[\text{S II}]\lambda 6716$ is not available (see Section 4.2).

Table 6
Element Abundance Ratios of the LRIS EMPG Candidates

#	ID	$\log(\text{Ne}/\text{O})$	$\log(\text{Ar}/\text{O})$	$\log(\text{N}/\text{O})$	$\log(\text{Fe}/\text{O})$
(1)	(2)	(3)	(4)	(5)	(6)
1	J0156–0421	$-0.759^{+0.021}_{-0.019}$	$-2.39^{+0.17}_{-0.25}$	$-1.22^{+0.10}_{-0.11}$	<–0.45
2	J0159–0622	$-0.878^{+0.017}_{-0.018}$	$-2.32^{+0.02}_{-0.02}$	$-1.47^{+0.03}_{-0.03}$	$-1.74^{+0.17}_{-0.28-0.22}$
3	J0210–0124	$-0.688^{+0.016}_{-0.017}$	$-2.37^{+0.02}_{-0.02}$	$-1.72^{+0.03}_{-0.03}$	<–1.75
4	J0214–0243	$-0.644^{+0.016}_{-0.018}$	<–3.25	$-1.51^{+0.03}_{-0.03}$	<–1.61
5	J0226–0517	$-0.664^{+0.016}_{-0.017}$	$-2.38^{+0.03}_{-0.03}$	$-1.51^{+0.06}_{-0.07}$	<–1.27
6	J0232–0248	$-0.692^{+0.018}_{-0.017}$	$-2.42^{+0.05}_{-0.06}$	$-1.79^{+0.10}_{-0.12}$	<–1.26
7	J1608+4337	$-0.653^{+0.017}_{-0.016}$	$-2.35^{+0.02}_{-0.03}$	$-1.47^{+0.02}_{-0.03}$	$-1.66^{+0.15}_{-0.22-0.20}$
8	J2236+0444	$-0.811^{+0.063}_{-0.066}$	<–1.98	<–1.26	<–0.57
9	J2321+0125	$-0.810^{+0.074}_{-0.064}$	<–1.76	<–0.68	<–0.07
10	J2355+0200	$-0.813^{+0.053}_{-0.051}$	<–2.00	<–1.13	<–0.52

Note. (1) Number. (2) ID. (3)–(6) Metal-to-oxygen abundance ratios in the gas phase. The upper limits represent 3σ confidence levels. The first and second terms of the Fe/O lower errors correspond to statistical and systematic errors, respectively. The systematic errors originated from the ICF uncertainty (Section 4.2).

phase element abundance ratios of the LRIS EMPG candidates are expected to be comparable to total element abundance ratios.

4.3. Stellar-mass Estimation

We estimate stellar masses with the spectral energy distribution (SED) interpretation code, BEAGLE (Chevallard & Charlot 2016). The BEAGLE code calculates both the stellar continuum and the nebular emission using the stellar population synthesis code (Bruzual & Charlot 2003) and the nebular emission library of Gutkin et al. (2016) that is computed with the photoionization code CLOUDY (Ferland et al. 2013). We adopt the Calzetti et al. (1994) law for the models for dust attenuation. Assuming a constant star formation history and the Chabrier (2003) IMF, we run the BEAGLE code with five free parameters of metallicity Z , maximum stellar age t_{max} , stellar mass M_* , ionization parameter U , and V -band optical depth τ_V . To obtain a parametric range of τ_V , we use the $\pm 68\%$ confidence intervals of $E(B - V)$ calculated in Section 4.1. Parametric

ranges of the other four parameters are $Z = 0.006\text{--}0.3 Z_\odot$, $\log(t_{\text{max}}/\text{yr}) = 4.0\text{--}9.0$, $\log(M_*/M_\odot) = 4.0\text{--}9.0$, and $\log(U) = (-2.5)\text{--}(-0.5)$, which are the same as those adopted in Paper III.²⁹ We use the redshift values obtained in Section 4.1. Because the HSC y -band image is ~ 1 mag shallower than the other broadband images, we do not use the HSC y -band data but the four-broadband ($griz$) data for the SED fitting. We use `cmodel` magnitudes of the $griz$ bands. Thanks to the deblending technique (Huang et al. 2018), the `cmodel` magnitude represents a total magnitude of a source even if overlaps with other sources. The $griz$ -`cmodel` magnitudes and stellar masses of the LRIS EMPG candidates are summarized in Table 7. In the table, we show only median values of the stellar masses because errors provided by the SED fitting do not include any uncertainty arising from different assumptions. This uncertainty is ~ 0.1 dex, which is larger than a typical error of ~ 0.05 dex provided by the SED fitting.

²⁹ When we fix Z and U based on our spectroscopic results of $12 + \log(\text{O}/\text{H})$ and $[\text{O III}]\lambda 5007/[\text{O II}]\lambda\lambda 3727, 3729$, we check that the M_* values change at most by ~ 0.3 dex, which does not change our conclusions.

Table 7
Stellar Masses of the LRIS EMPG Candidates

#	ID	<i>g</i> mag	<i>r</i> mag	<i>i</i> mag	<i>z</i> mag	$\log(M_*)$ M_\odot
(1)	(2)	(3)	(4)	(5)	(6)	(7)
1	J0156–0421	21.9	22.1	22.9	22.9	5.7
2	J0159–0622	18.3	18.6	19.3	19.2	5.4
3	J0210–0124	19.3	19.7	20.3	20.3	5.3
4	J0214–0243	19.1	19.4	20.0	20.2	6.1
5	J0226–0517	20.5	21.3	22.0	22.3	6.4
6	J0232–0248	20.3	20.8	21.4	21.7	5.9
7	J1608+4337	19.4	19.8	20.5	20.6	6.0
8	J2236+0444	22.3	22.2	22.8	22.9	5.2
9	J2321+0125	23.1	23.3	23.9	24.0	5.4
10	J2355+0200	21.1	21.1	22.4	22.4	4.8

Note. (1) Number. (2) ID. (3)–(6) HSC c_{model} magnitudes. (7) Stellar mass.

5. Results and Discussions

5.1. Metallicity

As listed in Table 6, 5 out of the 10 LRIS EMPG candidates (#1, 2, 8, 9, and 10) have low metallicities of $12 + \log(\text{O}/\text{H}) = 7.05\text{--}7.68$, which meet the EMPG criterion of $12 + \log(\text{O}/\text{H}) \leq 7.69$. We also conclude that four out of the other five LRIS EMPG candidates (#3, 5, 6, and 7) show a low metallicity of $12 + \log(\text{O}/\text{H}) = 7.73\text{--}7.78$ (i.e., 11%–12% $(\text{O}/\text{H})_\odot$). We thus refer to the nine (= 5 + 4) LRIS EMPG candidates with $\lesssim 10\%$ $(\text{O}/\text{H})_\odot$ as LRIS EMPGs. It should be noted that the other LRIS EMPG candidate (#4) still shows a low metallicity of $12 + \log(\text{O}/\text{H}) = 7.96$ (i.e., 19% $(\text{O}/\text{H})_\odot$). We emphasize that two of the LRIS EMPGs (#8 and 10) show extremely low metallicities of $12 + \log(\text{O}/\text{H}) = 6.93\text{--}7.35$ (i.e., 1.7–4.6% $(\text{O}/\text{H})_\odot$) including the 1σ uncertainties. The two LRIS EMPGs are thus the most metal-poor galaxies ever reported.

Figure 5 illustrates the mass–metallicity distributions of the LRIS EMPGs, the HSC spectroscopic EMPGs (see Section 2), and all the other EMPGs with $12 + \log(\text{O}/\text{H}) < 7.3$ (i.e., $< 4\%$ $(\text{O}/\text{H})_\odot$) determined by the direct- T_e method taken from the literature. The EMPGs from the literature are listed in Table 8. The mass–metallicity relation (MZR) of typical SFGs at $z \sim 0$ is well investigated and explained by the equilibrium of gas inflow/outflow and metal production by stars (e.g., Lilly et al. 2013). However, we confirm that EMPGs show a wide range of M_* from 10^4 to $10^8 M_\odot$, which implies that the equilibrium is not maintained at the low-mass (low-metallicity) end of the mass–metallicity distribution. Some EMPGs, including many of the LRIS EMPGs, lie above the extrapolation of the $z \sim 0$ MZR. Such EMPGs may be dominated by internal metal productions or outflows (Paper I) and be in the stage of transition from gas-rich dwarf irregulars to gas-poor dwarf spheroidals (Zahid et al. 2012). As part of the ongoing mid- to high-resolution spectroscopy survey with Magellan/MagE (EMPRESS-HRS; PI: M. Rauch), a subsequent EMPRESS paper (Xu et al. 2021) will report that EMPGs lying above the $z \sim 0$ MZR have broad components of emission lines with velocity widths of $\sim 200 \text{ km s}^{-1}$, which may be attributed to the outflow. On the other hand, some of the EMPGs from the literature lie below the extrapolation of the $z \sim 0$ MZR. In such EMPGs, the contribution of metal-poor gas inflow may overwhelm the contribution of internal metal productions as discussed in Hughes et al. (2013).

We also find that LRIS EMPGs #8 and #10 also show extremely low stellar masses of $5 \times 10^4\text{--}7 \times 10^5 M_\odot$. LRIS EMPGs #8 and #10 are helpful to understand the nature of galaxies in the very early-formation phase because there have been only ~ 7 EMPGs reported so far to have both $12 + \log(\text{O}/\text{H}) \lesssim 7.3$ and $M_* \lesssim 10^6 M_\odot$. We need to explore EMPGs continuously not only to identify the lowest-metallicity galaxies but also to verify whether there is a metallicity lower limit (a.k.a. metallicity floor; Prochaska et al. 2003) that local galaxies can take. Our spectroscopic observations for the EMPRESS sample continue to address the question. A recent follow-up identifies new EMPRESS EMPGs that have stellar mass as low as $M_* \sim 10^{4.7} M_\odot$ (K. Nakajima et al. 2021, in preparation). However, their metallicities do not fall below the currently known metallicity floor of $\sim 1\%$ of the solar metallicity (e.g., Thuan et al. 2005), supporting a deficit of galaxies with metallicities below $\sim 1\%$ in the local universe.

5.2. Element Abundance Ratio

Figure 6 shows the element abundance ratios of Ne/O, Ar/O, N/O, and Fe/O of the LRIS EMPGs and local metal-poor galaxies of Izotov (2006; gray) as functions of metallicity. As shown in the top two panels, the LRIS EMPGs show the α -element ratios of Ne/O and Ar/O comparable to the solar abundance ratios as well as other metal-poor galaxies.

The bottom-left panel of Figure 6 presents the relations between N/O and $12 + \log(\text{O}/\text{H})$, illustrating that local metal-poor galaxies present a plateau at $\log(\text{N}/\text{O}) \sim -1.6$ in the range of $12 + \log(\text{O}/\text{H}) \lesssim 8.0$ and a positive slope at $12 + \log(\text{O}/\text{H}) \gtrsim 8.0$. Various studies such as Vincenzo et al. (2016; hereafter V16) suggest that the plateau and the positive slope are attributed to the primary and the secondary nucleosyntheses in massive and low-mass stars, respectively. We find that some of the LRIS EMPGs lie on the plateau. Such EMPGs are not likely to be affected by the chemical enrichment of low-mass stars but rather by massive stars. We also find that LRIS EMPGs #3 and #6 lie below the plateau, showing very low N/O ratios of $\log(\text{N}/\text{O}) = (-1.7)\text{--}(-1.8)$. The two LRIS EMPGs may produce oxygen selectively rather than nitrogen due to top-heavy IMFs efficiently producing massive CCSNe or high star formation efficiencies (SFEs; defined as SFR normalized by gas mass) as discussed in Kumari et al. (2018).

The bottom-right panel of Figure 6 shows the relations between Fe/O and $12 + \log(\text{O}/\text{H})$. For the present case, we derive Fe/O for two out of the nine LRIS EMPGs (#2 and #7) from the $[\text{Fe III}]\lambda 4658$ line detection (Section 4.1). We find that LRIS EMPGs #2 and #7 have $\log(\text{Fe}/\text{O}) \sim -1.7$ and $\text{O}/\text{H} \sim 10\%$ $(\text{O}/\text{H})_\odot$. Adding the two LRIS EMPGs to the three EMPGs with Fe/O measurements (J1631+4426, J2115–1734, and J0811+4730) from the literature (Paper II; Izotov et al. 2018) represented by the magenta diamonds in the bottom-right panel of Figure 6, we now obtain a sample of five EMPGs with Fe/O measurements. We summarize the properties of the five EMPGs in Table 9. Even considering that the offsets originated from the ICF difference between Izotov (2006) and Rodriguez & Rubin (2005), we confirm that J1631+4426 and J0811+4730, having the lowest O/H ratios of $\sim 2\%$ $(\text{O}/\text{H})_\odot$, show $(\text{Fe}/\text{O})_\odot$, which is higher than that of the other three EMPGs with $\sim 10\%$ $(\text{O}/\text{H})_\odot$.

Based on the observations of quasar absorption systems, Becker et al. (2012) report that Fe/O ratios of the intergalactic medium

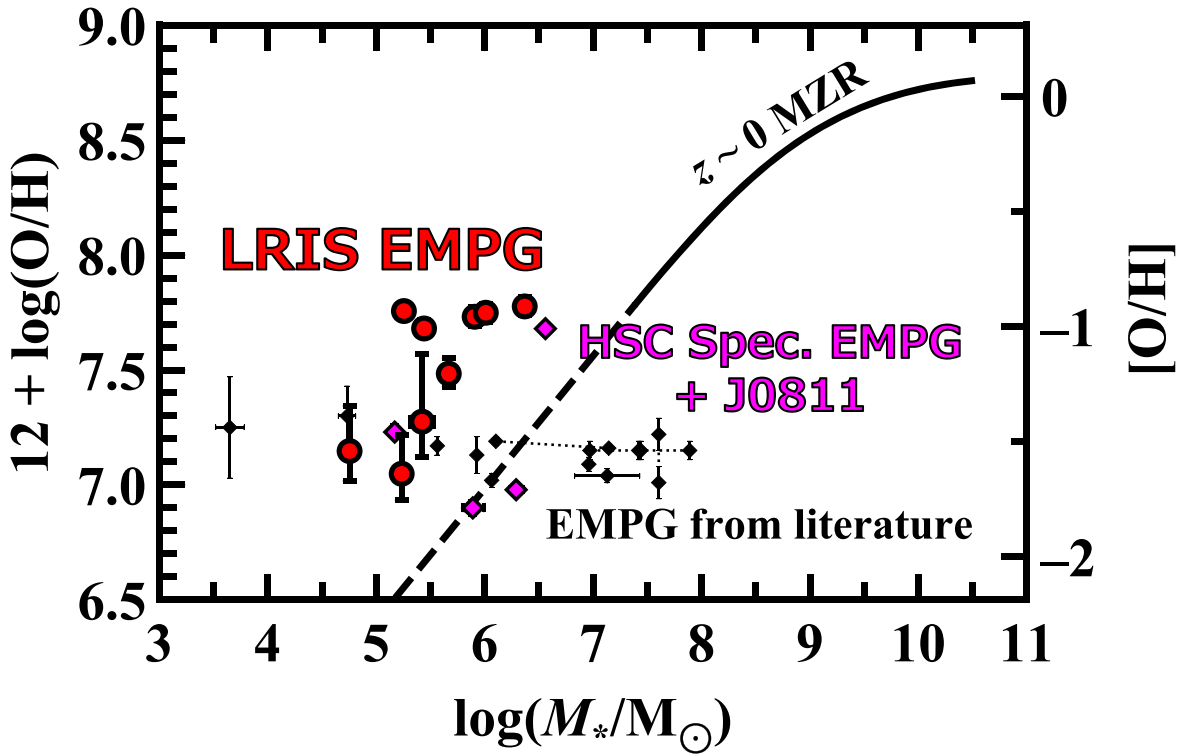


Figure 5. Mass–metallicity distribution of EMPGs. The red circles indicate the LRIS EMPGs (Section 5.1). We note that a typical uncertainty of M_* of the LRIS EMPGs is ~ 0.1 dex (Section 4.3). The magenta and black diamonds show the EMPGs listed in the upper and lower parts of Table 8, respectively. The black dotted lines connecting some of the black diamonds describe that these black diamonds represent individual clumps belonging to the same EMPGs. The black solid curve is the $z \sim 0$ mass–metallicity relation (MZR) from the SDSS using the same direct- T_c method (Andrews & Martini 2013). The black dashed line represents an extrapolation of the $z \sim 0$ MZR toward lower M_* .

(IGM) at $z \sim 2\text{--}6$ are almost constant at a value of $[\text{Fe}/\text{O}] \sim -0.4$ (i.e., $\log(\text{Fe}/\text{O}) \sim -1.6$). If the $z \sim 0$ IGM also has an Fe/O value of $[\text{Fe}/\text{O}] \sim -0.4$, we need some events such as SN explosions that enhance Fe/O ratios by $\gtrsim 0.4$ dex to explain high Fe/O ratios of J1631+4426 and J0811+4730. As discussed in Paper II, however, Type Ia SNe are less likely to be the main contributors to enhance the Fe/O ratios of J1631+4426 and J0811+4730 because of their low O/H and N/O ratios. We discuss the origin of the Fe/O enhancements quantitatively in Section 6.

6. Origin of Fe/O Enhancements

In this section, we revisit the origin of the high Fe/O ratio of J1631+4426 and J0811+4730 with $\sim 2\%$ $(\text{O}/\text{H})_{\odot}$, investigating possible contributors of HNe and PISNe that have not been discussed in Paper II (Section 1). We also re-explore the contribution of metal-poor gas inflow into EMPGs because such inflows probably trigger star-forming activities, whose effect has not been evaluated in Paper II.

6.1. Considerable SN

We quantitatively explore the origin of the high Fe/O abundance ratios with Fe/O evolution models including various SN yields. Before explaining the models, we introduce considerable SNe that would be responsible for Fe/O ratios of EMPGs.

Very massive stars with $\sim 140\text{--}300 M_{\odot}$ are expected to undergo thermonuclear explosions as known as PISNe (Heger & Woosley 2002). Such a massive star above $\sim 140 M_{\odot}$

requires extremely metal-poor environments to form due to the efficient wind mass loss (e.g., Langer et al. 2007; Hirano et al. 2014). Specifically, cores of stars with $\sim 200\text{--}300 M_{\odot}$ are mostly transformed into ^{56}Ni during the explosion (Takahashi et al. 2018). The ^{56}Ni atoms consequently decay to ^{56}Fe (Nadyozhin 1994), which largely contribute to the Fe/O enrichment. PISNe appear ~ 2 Myr after star formation, which corresponds to a lifetime of stars of $\sim 300 M_{\odot}$ (Takahashi et al. 2018).

Massive stars with $\sim 8\text{--}100 M_{\odot}$ evolve into neutron stars or black holes (BHs), undergoing CCSNe. Typical CCSNe are expected to produce low-Fe/O gas because α elements, including oxygen, are selectively created in massive stars during the α reaction (e.g., Nomoto et al. 2006). The CCSNe emerge ~ 3 Myr after star formation, which corresponds to a lifetime of stars of $100 M_{\odot}$ (Portinari et al. 1998).

Some massive stars with $\sim 30\text{--}100 M_{\odot}$ undergo CCSNe with explosion energies of $\gtrsim 10^{52}$ erg, which is ~ 1 dex larger than that of a typical CCSN of $\sim 10^{51}$ erg. Such CCSNe with high explosion energies are referred to as HNe (e.g., Iwamoto et al. 1998). The light-curve model for the observed HN SN 1998bw associated with GRB 980425 shows that the mass of Fe (mostly a decay product of radioactive ^{56}Ni) is $\sim 0.4 M_{\odot}$ (Nakamura et al. 2001). This HN model with $\sim 3 \times 10^{52}$ erg for SN 1998bw yields $[\text{Fe}/\text{O}] \sim -0.5$. By taking into account the observation and model of SN 1998bw, Nomoto et al. (2006, 2013) provided yield tables giving $[\text{Fe}/\text{O}] \sim -0.5$ from HNe. However, the amount of Fe in HN models depends on the explosion energy, the progenitor mass, and the mass cut that

Table 8
EMPGs from the Literature

Name (1)	$12 + \log(\text{O}/\text{H})$ (2)	$\log(M_*/M_\odot)$ (3)	Reference (4)
J1631+4426	6.90 ± 0.03	$5.89^{+0.10}_{-0.09}$	Paper I
J2314+0154	$7.23^{+0.03}_{-0.02}$	5.17 ± 0.01	Paper I
J2115-1734	7.68 ± 0.01	6.56 ± 0.02	Paper I
J0811+4730	6.98 ± 0.02	6.29 ± 0.06	Izotov et al. (2018)
AGC198691	7.02 ± 0.03	6.06	Hirschauer et al. (2016)
J1234+3901	7.04 ± 0.03	7.13 ± 0.3	Izotov et al. (2019)
J2229+2725	7.09 ± 0.03	6.96	Izotov et al. (2021)
Little Cub	7.13 ± 0.08	5.93	Hsyu et al. (2017)
Leo P	7.17 ± 0.04	5.56	Skillman et al. (2013)
J1005+3722	7.25 ± 0.22	3.65 ± 0.13	Senchyna & Stark (2019)
J0845+0131	7.30 ± 0.13	4.73 ± 0.08	Senchyna & Stark (2019)
SBS 0335#1	7.01 ± 0.07	(7.61)	Izotov et al. (2009)
SBS 0335#2	7.22 ± 0.07	(7.61)	Izotov et al. (2009)
DDO68#1	(7.15 ± 0.04)	7.44 ± 0.03	Sacchi et al. (2016)
DDO68#2	(7.15 ± 0.04)	7.89 ± 0.01	Sacchi et al. (2016)
DDO68#3	(7.15 ± 0.04)	7.42 ± 0.02	Sacchi et al. (2016)
DDO68#4	(7.15 ± 0.04)	6.97 ± 0.03	Sacchi et al. (2016)
I Zw 18NW	7.16 ± 0.01	7.14	Izotov & Thuan (1998)
I Zw 18SE	7.19 ± 0.02	6.10	Izotov & Thuan (1998)

Note. (1) Name. (2) $12 + \log(\text{O}/\text{H})$. (3) Stellar mass. We show errors of $12 + \log(\text{O}/\text{H})$ and M_* as long as they are reported in the literature. The values in the parentheses indicate that the metallicities or stellar masses are not derived for each individual clump. (4) Reference. In the upper part of this table, we list the HSC spectroscopic EMPGs (Paper I; Section 2) and J0811+4730 (Izotov et al. 2018). In the lower part of this table, we summarize other EMPGs with $12 + \log(\text{O}/\text{H}) < 7.3$ (i.e., $< 4\%$ $(\text{O}/\text{H})_\odot$).

divides the ejecta and the compact remnant. Umeda & Nomoto (2008) predict that HNe with high explosion energies tend to produce higher Fe/O gas even above the solar abundance because their high temperatures promote the nucleosynthesis of ^{56}Ni that is decaying into ^{56}Fe . In addition, when we set a low value of the mass cut, HNe with normal explosion energies of $\sim 1-3 \times 10^{52} \text{ erg s}^{-1}$ can also eject high Fe/O gas above the solar abundance (Umeda & Nomoto 2008). Because HNe that eject a large amount of (radioactive) ^{56}Ni should be bright, we refer to HNe with high explosion energies and/or low-mass cuts as bright HNe (BrHNe) hereafter. Shivvers et al. (2017) report that $\sim 1\%$ of observed CCSNe are HNe. However, Modjaz et al. (2020) report that galaxies hosting HNe tend to be metal poor, which implies that HNe are preferentially born in metal-poor environments.

Low- and intermediate-mass stars evolve into white dwarfs. If a white dwarf belongs to a binary system, the system may host a Type Ia SN. A delay time of Type Ia SNe, τ_{Ia} , is defined to be a time from the beginning of the star formation to the appearance of the first Type Ia SN. We assume that the minimum possible τ_{Ia} is 50 Myr (e.g., Mannucci et al. 2005; Sullivan et al. 2006), which is linked to the maximum zero-age main-sequence mass of stars that evolve into white dwarfs ($\sim 8 M_\odot$)³⁰. Type Ia SNe can eject high Fe/O gas above the solar abundance because carbon deflagrations in white dwarfs synthesize ^{56}Fe .

³⁰ Using observational data of SNe hosted by galaxies with old stellar populations, Totani et al. (2008) report a reasonable τ_{Ia} range of 0.1–10 Gyr.

6.2. Fe/O Evolution Model

To evaluate the contribution of Type Ia SNe, we use an Fe/O evolution model of Suzuki & Maeda (2018; hereafter SM18). We refer to this model as the Milky Way (MW) model because the model is calibrated by observations of absorptions of MW stars (e.g., Bensby et al. 2014). In the MW model, an Fe/O ratio at each age is defined as the ratio of the total numbers of iron and oxygen atoms produced by all SNe that have already exploded before that age. First, SM18 created stars based on an IMF of Kroupa (2001), which have mass slopes of -2.3 , -1.3 , and -0.3 for stars with $M \geq 0.5$, $0.08 < M < 0.5$, and $M \leq 0.08 M_\odot$, respectively. SM18 derived lifetimes of the stars as a function of star masses from Padovani & Matteucci (1993). SM18 assumed that all stars below $8 M_\odot$ and with $9-100 M_\odot$ evolve into white dwarfs and CCSNe, respectively, after finishing their lifetimes. The white dwarfs become Type Ia SNe following a delay-time distribution $D(t_d)$, which is proportional to t_d^{-1} and normalized so that the MW model reproduces $\text{Fe}/\text{O} = (\text{Fe}/\text{O})_\odot$ at the age of the formation of the Sun. SM18 used ejecta masses ($1.38 M_\odot$) and element yields of Type Ia SNe predicted by Nomoto et al. (1984). SM18 also adopted the metallicity-dependent CCSN yield of Limongi & Chieffi (2006) and the best-fit star formation history of the MW, whose SFR continuously increases until the age of ~ 800 Myr and decreases to the current SFR of the MW at the age of 13.8 Gyr.

Because the MW model does not take into account ejecta from HNe or PISNe, we construct new Fe/O evolution models incorporating HNe or PISNe. Again, it is important to evaluate contributions of HNe and PISNe to the Fe/O enhancements of young metal-poor galaxies because both occur much earlier than Type Ia SNe and also because they are preferentially born in the metal-poor environment (Langer et al. 2007; Modjaz et al. 2020). To examine whether HNe or PISNe can contribute to the Fe/O enhancements of EMPGs, we calculate Fe/O until the age of 50 Myr (i.e., before the first Type Ia SN appears). Other than this point, we construct the models in the same way as SM18. We use an IMF with a mass slope of -2.3 (a.k.a. Salpeter IMF; Salpeter 1955)³¹, which is common in local star-forming galaxies. Massive stars finish their lifetimes as main-sequence stars earlier than less-massive stars. We derive the lifetimes of the stars as a function of star masses from the combination of Portinari et al. (1998; for $6-120 M_\odot$ stars) and Takahashi et al. (2018; for $100-300 M_\odot$ stars). We calculate element ejections from CCSNe, HNe, and PISNe using the most metal-poor SN yields of Nomoto et al. (2006, 2013), and Takahashi et al. (2018), respectively. Because Nomoto et al. (2006, 2013) calculate yields of CCSNe and HNe with progenitor masses of 30 and $40 M_\odot$, we extrapolate the yields to CCSNe/HNe with progenitor masses of $100 M_\odot$. To create BrHNe ejecting gas with the highest Fe/O, we use yields of Umeda & Nomoto (2008) with the highest explosion energy and the lowest-mass cut just above the Fe core at a given progenitor star mass.

Table 10 summarizes the assumptions of our Fe/O evolution models. For all the models, we assume that (1) all stars with $9-30 M_\odot$ explode as CCSNe, (2) all stars with $100-140 M_\odot$ undergo direct collapse that ejects no element, and (3) the star formation occurs at once at the beginning of the galaxy

³¹ The Salpeter IMF is equal to that of Kroupa (2001) in the mass range of $\geq 0.5 M_\odot$.

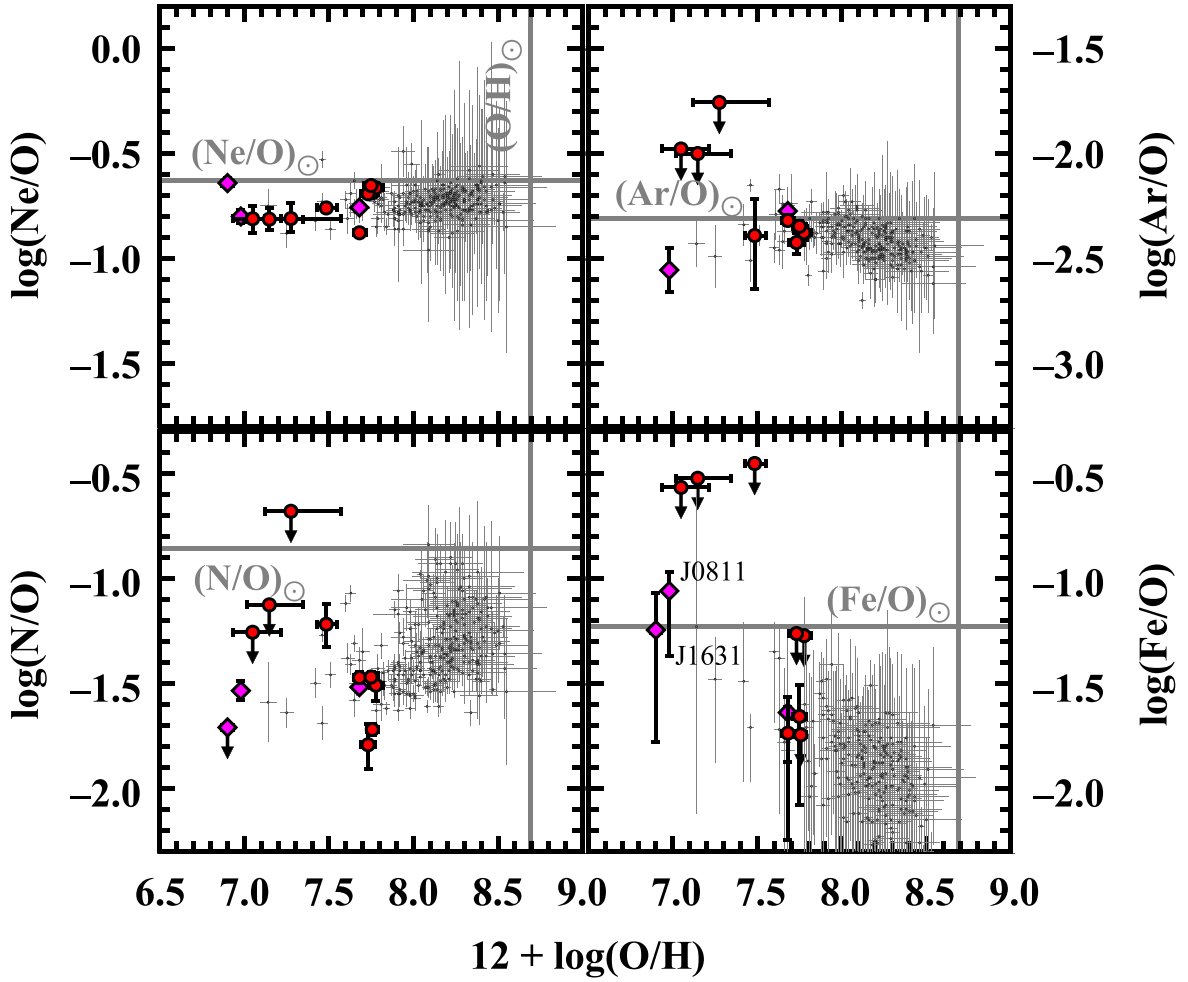


Figure 6. Gas-phase element abundance ratios of Ne/O (top left), Ar/O (top right), N/O (bottom left), and Fe/O (bottom right) as functions of $12 + \log(\text{O}/\text{H})$. The symbols are the same as in Figure 5. We also add local metal-poor galaxies (Izotov 2006) with the gray dots. We add 0.2 dex uncertainties to lower errors of Fe/O ratios of the local metal-poor galaxies because the Fe/O ratios are calculated from the ICF of Izotov et al. (2006; see Section 4.2). The gray solid lines represent the solar abundances (Asplund et al. 2021).

Table 9
EMPGs with Fe/O Measurements

Name	$12 + \log(\text{O}/\text{H})$	$\log(\text{Fe}/\text{O})$	$\log(\text{N}/\text{O})$	$\text{EW}_0(\text{H}\beta)$ Å	Reference
(1)	(2)	(3)	(4)	(5)	(6)
LRIS EMPG #2	$7.68^{+0.04}_{-0.03}$	$-1.74^{+0.17}_{-0.28-0.22}$	$-1.47^{+0.03}_{-0.03}$	127^{+83}_{-33}	This paper
LRIS EMPG #7	7.75 ± 0.04	$-1.66^{+0.15}_{-0.22-0.20}$	$-1.47^{+0.02}_{-0.03}$	83^{+44}_{-11}	This paper
J1631+4426	6.90 ± 0.03	$-1.25^{+0.17}_{-0.31-0.22}$	< -1.71	$123.5^{+3.5}_{-2.8}$	Papers I and II
J2115–1734	7.68 ± 0.01	$-1.64^{+0.03}_{-0.03-0.21}$	$-1.518^{+0.009}_{-0.011}$	$214.0^{+0.9}_{-0.8}$	Papers I and II
J0811+4730	6.98 ± 0.02	$-1.06^{+0.09}_{-0.09-0.22}$	-1.535 ± 0.044	282.0 ± 1.0	Izotov et al. (2018)

Notes. (1) Name. (2) $12 + \log(\text{O}/\text{H})$. (3) Fe/O. (4) N/O. (5) $\text{EW}_0(\text{H}\beta)$. (6) Reference.

formation (i.e., instantaneous star formation history). The percentages appeared in the model names of “HN 100%” and “BrHN 20%” represent how much fraction of stars with 30–100 M_{\odot} is assumed to undergo HNe and BrHNe, respectively. The other models (i.e., No HN/PISN and PISN models) assume that stars with 30–100 M_{\odot} undergo CCSNe.

Figure 7 illustrates the Fe/O evolution models, while we convert Fe/O to O/Fe normalized by the solar abundance

([O/Fe]). We find that the BrHN 20% (purple) and PISN (yellow) models show low O/Fe (high Fe/O) ratios comparable to the solar abundance during the \odot and \oplus eras. The HN 100% (blue), BrHN 20%, and PISN models show maximum O/Fe (minimum Fe/O) values at ~ 10 Myr mainly because the high-Fe/O gas produced by HNe or PISNe is diluted with the low-Fe/O gas efficiently ejected from CCSNe whose progenitor masses are $\gtrsim 20 M_{\odot}$. The MW model (cyan) predicts that

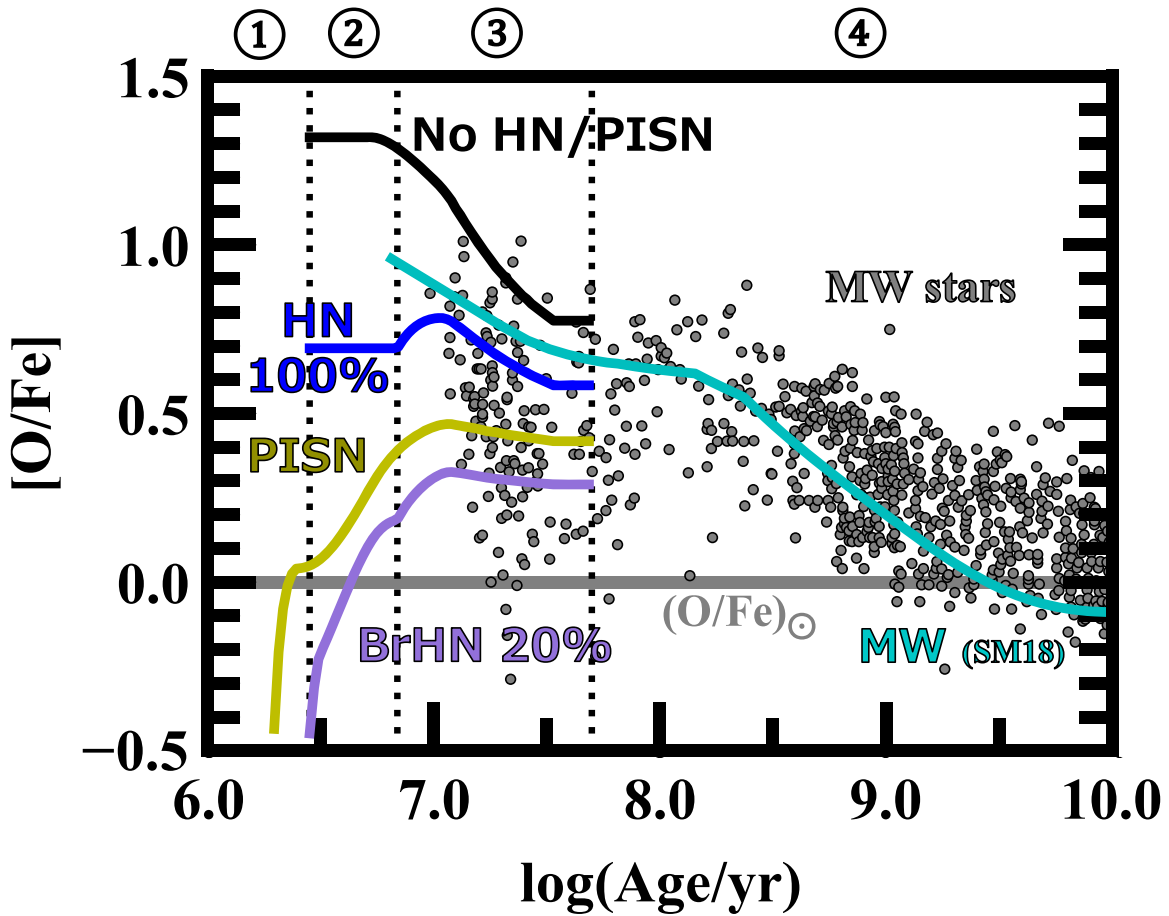


Figure 7. O/Fe evolution models. The cyan, black, blue, purple, and yellow curves indicate the MW, the No HN/PISN, the HN 100%, the BrHN 20%, and the PISN models, respectively. In Table 10, we summarize the assumptions of the models mentioned above. The gray dots show the MW stars (Edvardsson et al. 1993; Gratton et al. 2003; Reddy et al. 2003; Cayrel et al. 2004; Bensby et al. 2014; Roederer et al. 2014). The gray horizontal line indicates the solar abundance of O/Fe . From left to right, the vertical dotted lines show the lifetimes of stars with 100, 30, and $8 M_{\odot}$, respectively.

Table 10
Fe/O Evolution Models

Model Name	Mass Range M_{\odot}	Progenitor Star with			Yield of (Br)HN or PISN (6)
		9–30 M_{\odot} (3)	30–100 M_{\odot} (4)	140–300 M_{\odot} (5)	
(1) No HN/PISN	9–100	CCSN	CCSN
HN 100%	9–100	CCSN	HN	...	Nomoto et al. (2013)
BrHN 20%	9–100	CCSN	BrHN: 20% CCSN: 80%	...	Umeda & Nomoto (2008)
PISN	9–300	CCSN	CCSN	PISN	Takahashi et al. (2018)

Notes (1) Model name. The percentages represent how much fraction of stars with 30–100 M_{\odot} is assumed to undergo HNe (or BrHNe). (2) Mass range of progenitor stars. (3)–(5) SN evolved from stars with 9–30, 30–100, and 140–300 M_{\odot} . We assume that stars with 100–140 M_{\odot} undergo direct collapse (i.e., ejecting no gas). (6) Reference for the yields of HNe, BrHNe, or PISNe. Regarding CCSNe, we use the yield of Nomoto et al. (2006). We also adopt the Salpeter IMF and the instantaneous star formation history for all the models.

the O/Fe (Fe/O) value continuously decreases (increases) with age. The decrease in O/Fe (increase in Fe/O) during the ④ era is mainly attributed to Type Ia SNe³².

The gray dots in Figure 7 show the distribution of the MW stars (Edvardsson et al. 1993; Gratton et al. 2003; Reddy et al. 2003;

Cayrel et al. 2004; Bensby et al. 2014; Roederer et al. 2014). Because we cannot determine the $[Fe/H]$ evolutions of the (Br)HN/PISN models due to uncertainties of the evolution models of gas masses (and thus hydrogen abundances) of EMPGs, we convert the $[Fe/H]$ of the MW stars to age using the $[Fe/H]$ evolution models of SM18 instead. The MW model reproduces the distribution of the MW stars especially during the ④ era (i.e., $[Fe/H] \gtrsim -2$), which indicates that the contribution of Type Ia SNe is properly incorporated into the MW model. In the ③ era (i.e., $[Fe/H] \lesssim -2$), however, the

³² All of the models predict that O/Fe values decrease (Fe/O values increase) with age during the ④ era because CCSNe whose progenitor masses are less than $\sim 18 M_{\odot}$ (a.k.a. Type IIP SNe) produce Fe/O higher than those ejected from more-massive CCSNe (SM18).

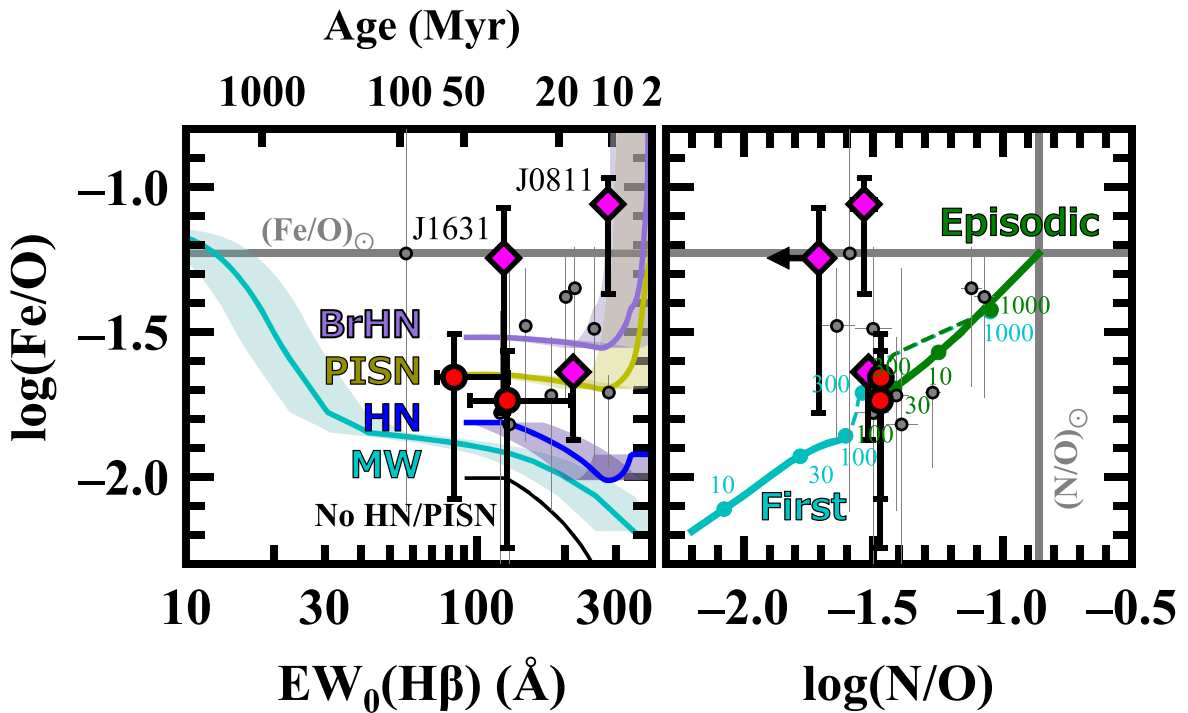


Figure 8. Fe/O ratio as a function of $EW_0(H\beta)$ and N/O described in the left and right panels, respectively. The gray circles indicate local metal-poor galaxies (Izotov 2006), which are the same as in Figure 6 but limited to those with $12 + \log(O/H) \leq 7.69$. Regarding the local metal-poor galaxies (Izotov 2006), we only show errors of Fe/O. The other symbols are the same as in Figure 6 but limited to those with Fe/O measurements or strong upper limits of Fe/O. In the left panel, the cyan, blue, purple, and yellow curves with the shaded regions show the MW, the HN 100%, the BrHN 20%, and the PISN models, respectively. The black curve indicates the No HN/PISN model. In the right panel, the cyan and green curves represent evolution tracks of Fe/O and N/O when first and episodic starbursts occur in a galaxy, respectively. The numbers accompanied by the curves indicate the ages in the unit of Myr. We draw the evolution tracks with solid and dashed lines before and after 100 Myr, respectively, because all the EMPGs shown in the left panel have ages $\lesssim 100$ Myr. To predict Fe/O and N/O ratios, we use the MW model (SM18) and the V16 model, respectively. The gray lines show the solar abundances (Asplund et al. 2021).

MW model cannot explain the distribution of the MW stars with low O/Fe (high Fe/O) ratios. The BrHN and the PISN models reproduce the distribution of the MW stars with low O/Fe ratios of $[O/Fe] = 0.3-0.4$, which implies that some metal-poor stars contain elements from HNe or PISNe as discussed in Aoki et al. (2014). We may need HNe or PISNe other than Type Ia SNe or CCSNe to reproduce the chemical enrichment of galaxies in the early-formation phase.

Finally, we convert the model age to $EW_0(H\beta)$ because the stellar age used in the models is not observable. Using the BEAGLE code calculating both the stellar continuum and the nebular emission (cf. Section 4.3), Paper I derives $EW_0(H\alpha)$ as a function of stellar age and $12 + \log(O/H)$ under the assumption of the constant star formation. Basically, the $EW_0(H\alpha)$ increases as $12 + \log(O/H)$ decreases because metal-poor stars make stellar continua harder (e.g., Tumlinson & Shull 2000). To remove the $12 + \log(O/H)$ dependency, we assume a relation between O/H and the stellar age of the MW model (SM18). Using the empirical relation of $EW_0(H\alpha) = 5.47 \times EW_0(H\beta)$; Paper I), we obtain a relation between $EW_0(H\beta)$ and the stellar age.

Here we evaluate the uncertainty in the conversion from the stellar age to $EW_0(H\beta)$. Paper I and Izotov et al. (2018) report that J1631+4426 and J0811+4730 have stellar ages of 50 and 3.3 Myr and $EW_0(H\beta)$ of 120 and 280 Å, respectively. Using the relation between $EW_0(H\beta)$ and the stellar age, we find that the stellar ages of 50 and 3.3 Myr correspond to $EW_0(H\beta)$ of 90 and 380 Å, respectively. The stellar ages inferred from $EW_0(H\beta)$ are different from those in the literature by ~ 0.13 dex. Thus, we add

the ± 0.13 dex uncertainties to the $EW_0(H\beta)$ values of the Fe/O evolution models.

Although the models provide total (= gas + dust + stellar) Fe/O ratios, we note that the gas-phase Fe/O ratios of dust-poor and low- M_* EMPGs are expected to be comparable to the total Fe/O ratios (and thus the Fe/O ratios predicted by the models) because we can ignore the amount of SN ejecta trapped in dust grains and stars.

6.3. Possible Scenario

To explain the Fe/O enhancements, we investigate three scenarios: 1) Type Ia SN, 2) gas dilution and episodic star formation, and 3) HN, BrHN, or PISN.

6.3.1. Type Ia SN

First, we quantitatively check whether Type Ia SNe are not responsible for the Fe/O enhancements as concluded by Paper II. Below, we use the MW model (SM18), in which only Type Ia SNe can eject iron-rich gas. In the left panel of Figure 8, we show the MW model represented by the cyan curve with the shaded region, respectively. The Fe/O value increases as the $EW_0(H\beta)$ value decreases (and thus the age increases) especially in the range of $EW_0(H\beta) \lesssim 50$ Å (i.e., $\gtrsim 100$ Myr) because of the appearance of Type Ia SNe.

We find that J0811+4730 shows an Fe/O value significantly higher than the MW model prediction with a little uncertainty. J0811+4730 has a large $EW_0(H\beta)$ of ~ 300 Å corresponding to an extremely young age of ~ 10 Myr, which suggests that Type Ia SNe, whose minimum possible delay time is 50 Myr

(Section 6.1), cannot contribute to the Fe/O enhancement of J0811+4730. Thus, we can rule out the first scenario for J0811+4730. We can also reject the possibility that the Fe/O value of J1631+4426 is consistent with the MW model to at least the $\sim 1\sigma$ level. In addition, the Fe/O excess of J1631+4426 from the MW model may become larger because J1631+4426 has an EMPG-tail (Paper III; see Section 3.1), which potentially makes the EW of J1631+4426 underestimated by a factor of 2 (Section 4.1). We thus conclude that the Fe/O enhancement of J1631+4426 is not likely to be attributed to Type Ia SNe.

Relations between the Fe/O and N/O of J1631+4426 and J0811+4730 also support the conclusion mentioned above. To estimate the N/O enrichment, we utilize a chemical evolution model of V16. Because V16 implemented the primary nucleosynthesis of nitrogen in massive stars (Romano et al. 2010), the V16 model can reproduce the observed relation between the N/O and $12 + \log(\text{O}/\text{H})$ of local star-forming galaxies within a wide metallicity range of $12 + \log(\text{O}/\text{H}) \sim 7.2\text{--}8.7$. In the right panel of Figure 8, we show the evolution tracks of the relation between Fe/O and N/O based on the MW model (SM18) and the V16 model represented by the cyan solid curve. We find that J0811+4730 and J1631+4426 have very high Fe/O and low N/O ratios, which cannot be reproduced by the first star formation model. We conclude again that Type Ia SNe are not likely to enhance the Fe/O ratios of J0811+4730 and J1631+4426.

We note that the EMPGs other than J0811+4730 or J1631+4426 also have young ages of < 100 Myr inferred from their large $\text{EW}_0(\text{H}\beta)$ as shown in the left panel of Figure 8. However, none of the EMPGs are consistent with the first star formation model with ages less than 100 Myr as illustrated in the right panel of Figure 8. This indicates that Type Ia SNe are not responsible for Fe/O ratios of typical EMPGs.

6.3.2. Gas Dilution and Episodic Star Formation

The second scenario is a combination of gas dilution and episodic star formation caused by primordial gas inflow. Paper III reports that more than 80% of EMPGs have EMPG-tails. Sánchez Almeida et al. (2015) report that EMPG-tails have O/H ratios ~ 1 dex larger than those of EMPGs, which suggest that metal-poor gas accretion onto EMPG-tails triggers star formation activities of EMPGs. If EMPGs and EMPG-tails originally share the same gas, it is possible that the EMPGs have high-Fe/O gas produced by past star formations in the EMPG-tails.

In this section, we assume that EMPGs originally have all element abundances equal to the solar abundances based on the fact that a typical EMPG-tail has $\text{O}/\text{H} \sim (\text{O}/\text{H})_\odot$ (Sánchez Almeida et al. 2015). Then, we investigate how element abundance ratios of the EMPGs change after the metal-poor gas inflow into the EMPGs. If the $z \sim 0$ IGM also has an Fe/O ratio of $[\text{Fe}/\text{O}] \sim -0.4$, comparable to those at $z \gtrsim 2$ (Becker et al. 2012), an IGM-gas inflow onto an EMPG may decrease the Fe/O of the EMPG. However, the decline is probably negligible because the IGM metallicity in the local universe may have a lower limit of $\sim 10^{-2} Z_\odot$ (e.g., Thuan et al. 2005). For the sake of simplicity, we assume primordial (i.e., only hydrogen) gas inflow. Just after the original gas components of the EMPGs are diluted with the primordial gas, metal-to-hydrogen ratios such as $12 + \log(\text{O}/\text{H})$ decrease while Fe/O ratios remain comparable to $(\text{Fe}/\text{O})_\odot$. However, N/O ratios should also be similar to $(\text{N}/\text{O})_\odot$, whereas the EMPGs have

N/O ratios significantly lower than $(\text{N}/\text{O})_\odot$ as described in the bottom-left panel of Figure 6. Thus, the dilution of the solar-metallicity gas by the primordial gas cannot explain the Fe/O enhancements of the EMPGs by itself as discussed in Paper II.

However, the primordial gas inflow can trigger episodic star formation, which potentially impacts element abundance ratios of the whole EMPG due to its low stellar mass. The N/O ratio is expected to decrease until ~ 100 Myr after the episodic star formation because massive stars produce low-N/O gas of $\sim 20\%$ $(\text{N}/\text{O})_\odot$ (V16). Thus, we investigate the contribution of the episodic star formation, which has not been investigated in Paper II. As in Section 6.3.1, we adopt the MW model and the V16 model to predict Fe/O and N/O evolutions, respectively. Assuming that the inflow quintuples the gas mass of the galaxy after finishing the first major star formation, we calculate the evolution track of the episodic starburst as shown in the right panel of Figure 8 with the green solid curve.

Regarding J1631+4426 and J0811+4730, we identify that even the episodic star formation model cannot reproduce the high Fe/O, the low N/O, and the young ages of $\lesssim 50$ Myr at the same time. Of course, we can create episodic star formation models that satisfy the high Fe/O, the low N/O, and the young ages of the EMPGs by arbitrarily assuming that the EMPGs originally have high Fe/O and low N/O ratios. However, such an assumption is unlikely to be plausible because the first burst model at any age does not reproduce high Fe/O and low N/O ratios simultaneously. We conclude that the second scenario can be ruled out for J1631+4426 and J0811+4730 even if the inflow triggers the episodic starburst.

We note that many of the EMPGs other than J1631+4426 or J0811+4730 have relatively high Fe/O and N/O ratios comparable to those predicted by the episodic star formation model within the range of < 100 Myr. These EMPGs may have old gas populations that are already affected by Type Ia SNe and AGB stars as discussed in Sánchez Almeida et al. (2016).

6.3.3. HN, BrHN, or PISN

The third scenario is the contribution of HNe, BrHNe, or PISNe, which has not been investigated in Paper II. The left panel of Figure 8 illustrates the models containing HNe, BrHNe, or PISNe (Table 10). We find that either the BrHN 20% (purple) or the PISN (yellow) models can reproduce the relations between the Fe/O and $\text{EW}_0(\text{H}\beta)$ of J1631+4426 and J0811+4730. We also find that we cannot explain the Fe/O enhancements even with the HN 100% model (blue), which implies that HNe with relatively-low explosion energies of $\sim 10^{52}$ erg and reasonable mass cuts are not responsible for the Fe/O enhancements. We conclude that BrHNe or PISNe can contribute to the Fe/O enhancements of J1631+4426 and J0811+4730. The N/O ratio potentially isolates BrHNe from PISNe. We need BrHN and PISN yields that plausibly calculate the primary nucleosynthesis of nitrogen as implemented in V16.

We note that most of the EMPGs in Figure 8 are also in agreement with either the BrHN 20% or the PISN models. This may trace the (past) presence of BrHNe or PISNe in the EMPGs (with moderate Fe/O ratios). Some of the EMPGs have low Fe/O ratios comparable to those predicted by the HN 100% model. Such EMPGs may be affected by (normal) HNe.

One may wonder whether the presence of BrHNe or PISNe conflicts with the positive trend between the O/Fe and Fe/H ratios of MW stars (as well as stars in satellite galaxies of the

MW; e.g., Pompéia et al. 2008), which gives observational support to a cosmic clock. However, the positive trend is clear only within the range of $[\text{Fe}/\text{H}] \gtrsim -2$, which corresponds to the formation age of the MW of $\gtrsim 50$ Myr in Figure 7. Stars below $[\text{Fe}/\text{H}] \lesssim -2$ (the formation age of the MW less than ~ 50 Myr) show a wide range of $[\text{O}/\text{Fe}]$ from ~ -0.3 to 1.0, which allows the presence of BrHNe or PISNe (see Section 6.2).

6.3.4. Conclusion

We have investigated the three scenarios that can explain the Fe/O enhancements of J1631+4426 and J0811+4730 with $\sim 2\%$ $(\text{O}/\text{H})_{\odot}$ and low N/O ratios. We conclude that the Fe/O enhancements are not likely to be explained by the Type Ia SN or the episodic star formation scenarios but by an inclusion of BrHNe and/or PISNe. This conclusion implies that first galaxies at $z \sim 10$ with metallicities of 0.1%–1% Z_{\odot} (Wise et al. 2012) could also have high Fe/O ratios because HNe and PISNe are preferentially produced in metal-poor environments (Section 6.1). Our conclusion also suggests that galaxies with high Fe/O ratios are not necessarily old enough to be affected by Type Ia SNe. This infers that Fe/O would not serve as a cosmic clock in primordial galaxies because it is not Type Ia SNe but HNe or PISNe that are likely to be responsible for the Fe/O enhancements in young metal-poor galaxies.

We note that Fe/O ratios of the EMPGs other than J1631+4426 or J0811+4730 can be generally explained by either episodic star formation or (Br)HNe/PISNe due to their moderate Fe/O and N/O ratios compared with J1631+4426 and J0811+4730. Primordial galaxies such as J1631+4426 and J0811+4730 are thus important to verify the presence of BrHNe or PISNe.

7. Summary

We present element abundance ratios of local EMPGs, which are expected to be galaxies in the early-formation phase. We conduct spectroscopic follow-up observations for 13 faint EMPG candidates selected by EMPRESS with Keck/LRIS. We newly identify nine EMPGs with $\text{O}/\text{H} = 2.2\text{--}12\%$ $(\text{O}/\text{H})_{\odot}$ at $z = 0.009\text{--}0.057$. Notably, two out of the nine EMPGs have extremely low stellar masses and oxygen abundances of $5 \times 10^4\text{--}7 \times 10^5 M_{\odot}$ and $2\%\text{--}3\%$ $(\text{O}/\text{H})_{\odot}$, respectively, indicating that the two EMPGs are galaxies in the very early-formation phase. Comparing nucleosynthesis models with representative EMPGs, we pinpoint J1631+4426 and J0811+4730 as having the lowest O/H ratios of $\sim 2\%$ $(\text{O}/\text{H})_{\odot}$, whose high Fe/O and low N/O ratios cannot be explained by Type Ia SNe or episodic star formation but by BrHNe (Section 6.1) and/or PISNe. Because HNe and PISNe are preferentially produced in metal-poor environments, primordial galaxies at $z \sim 10$ as well as EMPGs potentially have high Fe/O values. We also suggest that the Fe/O ratio may not serve as a cosmic clock for primordial galaxies.

We thank the referee for the valuable comments. We are also grateful to Koh Takahashi, Nozomu Tominaga, Chiaki Kobayashi, Yutaka Hirai, and Daichi Kashino for having useful discussions. This paper includes data gathered with the 10 m Keck Telescope located at W. M. Keck Observatory, Hawaii. We thank the staff of Keck Observatory for their help with the observations. The Hyper Suprime-Cam (HSC) collaboration includes the astronomical communities of Japan

and Taiwan, and Princeton University. The HSC instrumentation and software were developed by the National Astronomical Observatory of Japan (NAOJ), the Kavli Institute for the Physics and Mathematics of the Universe (Kavli IPMU), the University of Tokyo, the High Energy Accelerator Research Organization (KEK), the Academia Sinica Institute for Astronomy and Astrophysics in Taiwan (ASIAA), and Princeton University. Based on data collected at the Subaru Telescope and retrieved from the HSC data archive system, which is operated by the Subaru Telescope and Astronomy Data Center at NAOJ. This work was supported by the joint research program of the Institute for Cosmic Ray Research (ICRR), University of Tokyo. The Cosmic Dawn Center is funded by the Danish National Research Foundation under grant No. 140. S.F. acknowledges support from the European Research Council (ERC) Consolidator Grant funding scheme (project ConText, grant No. 648179). This project has received funding from the European Union’s Horizon 2020 research and innovation program under the Marie Skłodowska-Curie grant agreement No. 847523 “INTERACTIONS.” This work is supported by World Premier International Research Center Initiative (WPI Initiative), MEXT, Japan, as well as the KAKENHI Grant-in-Aid for Scientific Research (A; 15H02064, 17H01110, 17H01114, 20H00180, and 21H04467) through the Japan Society for the Promotion of Science (JSPS). This work has been supported in part by JSPS KAKENHI grant Nos. JP17K05382, JP20K04024, and JP21H04499 (K.N.). Yuki Isobe, Kimihiko Nakajima, Yuichi Harikane, Takashi Kojima, and Masato Onodera are supported by JSPS KAKENHI grant Nos. 21J20785, 20K22373, 19J01222, 18J12840, and 17K14257, respectively.

ORCID iDs

Yuki Isobe  <https://orcid.org/0000-0001-7730-8634>
 Masami Ouchi  <https://orcid.org/0000-0002-1049-6658>
 Akihiro Suzuki  <https://orcid.org/0000-0002-7043-6112>
 Takashi J. Moriya  <https://orcid.org/0000-0003-1169-1954>
 Kimihiko Nakajima  <https://orcid.org/0000-0003-2965-5070>
 Ken’ichi Nomoto  <https://orcid.org/0000-0001-9553-0685>
 Yuichi Harikane  <https://orcid.org/0000-0002-6047-430X>
 Takashi Kojima  <https://orcid.org/0000-0001-5780-1886>
 Yoshiaki Ono  <https://orcid.org/0000-0001-9011-7605>
 Seiji Fujimoto  <https://orcid.org/0000-0001-7201-5066>
 Akio K. Inoue  <https://orcid.org/0000-0002-7779-8677>
 Ji Hoon Kim  <https://orcid.org/0000-0002-1418-3309>
 Yutaka Komiyama  <https://orcid.org/0000-0002-3852-6329>
 Haruka Kusakabe  <https://orcid.org/0000-0002-3801-434X>
 Chien-Hsiu Lee  <https://orcid.org/0000-0003-1700-5740>
 Michael Maseda  <https://orcid.org/0000-0003-0695-4414>
 Jorryt Matthee  <https://orcid.org/0000-0003-2871-127X>
 Tohru Nagao  <https://orcid.org/0000-0002-7402-5441>
 Themiyi Nanayakkara  <https://orcid.org/0000-0003-2804-0648>
 Moka Nishigaki  <https://orcid.org/0000-0003-4321-0975>
 Masato Onodera  <https://orcid.org/0000-0003-3228-7264>
 Yuma Sugahara  <https://orcid.org/0000-0001-6958-7856>
 Yi Xu  <https://orcid.org/0000-0002-5768-8235>

References

- Aihara, H., AlSayyad, Y., Ando, M., et al. 2019, *PASJ*, 71, 114
 Andrews, B. H., & Martini, P. 2013, *ApJ*, 765, 140
 Aoki, W., Tominaga, N., Beers, T. C., Honda, S., & Lee, Y. S. 2014, *Sci*, 345, 912
 Asplund, M., Amarsi, A. M., & Grevesse, N. 2021, *A&A*, 653, A141

- Becker, G. D., Sargent, W. L. W., Rauch, M., & Carswell, R. F. 2012, *ApJ*, **744**, 91
- Behroozi, P. S., Wechsler, R. H., & Conroy, C. 2013, *ApJ*, **770**, 57
- Bèland, S., Boulade, O., & Davidge, T. 1988, *BCFHT*, **19**, 16
- Bensby, T., Feltzing, S., & Oey, M. S. 2014, *A&A*, **562**, A71
- Berg, D. A., Erb, D. K., Henry, R. B. C., Skillman, E. D., & McQuinn, K. B. W. 2019, *ApJ*, **874**, 93
- Berg, D. A., Skillman, E. D., Croxall, K. V., et al. 2015, *ApJ*, **806**, 16
- Bruzual, G., & Charlot, S. 2003, *MNRAS*, **344**, 1000
- Calzetti, D., Armus, L., Bohlin, R. C., et al. 2000, *ApJ*, **533**, 682
- Calzetti, D., Kinney, A. L., & Storchi-Bergmann, T. 1994, *ApJ*, **429**, 582
- Cayrel, R., Depagne, E., Spite, M., et al. 2004, *A&A*, **416**, 1117
- Chabrier, G. 2003, *PASP*, **115**, 763
- Chevallard, J., & Charlot, S. 2016, *MNRAS*, **462**, 1415
- Edvardsson, B., Andersen, J., Gustafsson, B., et al. 1993, *A&A*, **500**, 391
- Ferland, G. J., Porter, R. L., van Hoof, P. A., et al. 2013, *RMxAA*, **49**, 137
- Froese Fischer, C., & Tachiev, G. 2004, *ADNDT*, **87**, 1
- Gardner, J. P., Mather, J. C., Clampin, M., et al. 2006, *SSRv*, **123**, 485
- Garnett, D. R. 1992, *AJ*, **103**, 1330
- Gratton, R. G., Carretta, E., Claudi, R., Lucatello, S., & Barbieri, M. 2003, *A&A*, **404**, 187
- Gutkin, J., Charlot, S., & Bruzual, G. 2016, *MNRAS*, **462**, 1757
- Hees, a., Hestroffer, D., Poncin-Lafitte, C. L., & David, P. 2015, *RAA*, **15**, 1945
- Heger, A., & Woosley, S. E. 2002, *ApJ*, **567**, 532
- Hirano, S., Hosokawa, T., Yoshida, N., et al. 2014, *ApJ*, **781**, 60
- Hirano, S., Hosokawa, T., Yoshida, N., Omukai, K., & Yorke, H. W. 2015, *MNRAS*, **448**, 568
- Hirschauer, A. S., Salzer, J. J., Skillman, E. D., et al. 2016, *ApJ*, **822**, 108
- Hsyu, T., Cooke, R. J., Prochaska, J. X., & Bolte, M. 2017, *ApJL*, **845**, L22
- Hsyu, T., Cooke, R. J., Prochaska, J. X., & Bolte, M. 2018, *ApJ*, **863**, 134
- Huang, S., Leauthaud, A., Murata, R., et al. 2018, *PASJ*, **70**, S6
- Hughes, T. M., Cortese, L., Boselli, A., Gavazzi, G., & Davies, J. I. 2013, *A&A*, **550**, A115
- Inoue, A. K. 2011, *MNRAS*, **415**, 2920
- Isobe, Y., Ouchi, M., Kojima, T., et al. 2021, *ApJ*, **918**, 54
- Iwamoto, K., Mazzali, P. A., Nomoto, K., et al. 1998, *Natur*, **395**, 672
- Izotov, Y. I., Guseva, N. G., Fricke, K. J., & Papaderos, P. 2009, *A&A*, **503**, 61
- Izotov, Y. I., Stasińska, G., Meynet, G., Guseva, N. G., & Thuan, T. X. 2006, *A&A*, **448**, 955
- Izotov, Y. I., & Thuan, T. X. 1998, *ApJ*, **497**, 227
- Izotov, Y. I., Thuan, T. X., & Guseva, N. G. 2019, *MNRAS*, **483**, 5491
- Izotov, Y. I., Thuan, T. X., & Guseva, N. G. 2021, *MNRAS*, **504**, 3996
- Izotov, Y. I., Worseck, G., Schaerer, D., et al. 2018, *MNRAS*, **478**, 4851
- James, B. L., Koposov, S., Stark, D. P., et al. 2015, *MNRAS*, **448**, 2687
- James, B. L., Koposov, S. E., Stark, D. P., et al. 2017, *MNRAS*, **465**, 3977
- Johansson, S., Zethson, T., Hartman, H., et al. 2000, *A&A*, **361**, 977
- Kikuchi-hara, S., Ouchi, M., Ono, Y., et al. 2020, *ApJ*, **893**, 60
- Kisielius, R., Storey, P. J., Ferland, G. J., & Keenan, F. P. 2009, *MNRAS*, **397**, 903
- Kojima, T., Ouchi, M., Rauch, M., et al. 2020, *ApJ*, **898**, 142
- Kojima, T., Ouchi, M., Rauch, M., et al. 2021, *ApJ*, **913**, 22
- Kroupa, P. 2001, *MNRAS*, **322**, 231
- Kumari, N., James, B. L., Irwin, M. J., Amorín, R., & Pérez-Montero, E. 2018, *MNRAS*, **476**, 3793
- Langer, N., Norman, C. A., de Koter, A., et al. 2007, *A&A*, **475**, L19
- Lilly, S. J., Carollo, C. M., Pipino, A., Renzini, A., & Peng, Y. 2013, *ApJ*, **772**, 119
- Limongi, M., & Chieffi, A. 2006, *ApJ*, **647**, 483
- Luridiana, V., Morisset, C., & Shaw, R. A. 2015, *A&A*, **573**, A42
- Mannucci, F., Valle, M. D., & Panagia, N. 2005, *A&A*, **433**, 807
- McLaughlin, B. M., & Bell, K. L. 2000, *JPhB*, **33**, 597
- Modjaz, M., Bianco, F. B., Siwek, M., et al. 2020, *ApJ*, **892**, 153
- Morales-Luis, A. B., Sánchez Almeida, J., Aguerri, J. A., & Muñoz-Tuñón, C. 2011, *ApJ*, **743**, 77
- Munoz Burgos, J. M., Loch, S. D., Ballance, C. P., & Boivin, R. F. 2009, *A&A*, **500**, 1253
- Nadyozhin, D. K. 1994, *ApJS*, **92**, 527
- Nakamura, T., Mazzali, P. A., Nomoto, K., & Iwamoto, K. 2001, *ApJ*, **550**, 991
- Nomoto, K., Kobayashi, C., & Tominaga, N. 2013, *ARA&A*, **51**, 457
- Nomoto, K., Thielemann, F. K., & Yokoi, K. 1984, *ApJ*, **286**, 644
- Nomoto, K., Tominaga, N., Umeda, H., Kobayashi, C., & Maeda, K. 2006, *NuPhA*, **777**, 424
- Oke, J. B., Cohen, J. G., Carr, M., et al. 1995, *PASP*, **107**, 375
- Oke, J. B., & Gunn, J. E. 1983, *ApJ*, **266**, 713
- Ono, Y., Ouchi, M., Harikane, Y., et al. 2018, *PASJ*, **70**, S10
- Padovani, P., & Matteucci, F. 1993, *ApJ*, **416**, 26
- Pompéia, L., Hill, V., Spite, M., et al. 2008, *A&A*, **480**, 379
- Portinari, L., Chiosi, C., & Bressan, A. 1998, *A&A*, **334**, 505
- Prochaska, J. X., Gawiser, E., Wolfe, A. M., Castro, S., & Djorgovski, S. G. 2003, *ApJ*, **595**, L9
- Pustilnik, S. A., Kniazev, A. Y., & Pramskij, A. G. 2005, *A&A*, **443**, 91
- Quinet, P. 1996, *A&AS*, **116**, 573
- Reddy, B. E., Tomkin, J., Lambert, D. L., & Allende Prieto, C. 2003, *MNRAS*, **340**, 304
- Rodríguez, M., & Rubin, R. H. 2005, *ApJ*, **626**, 900
- Roederer, I. U., Preston, G. W., Thompson, I. B., et al. 2014, *AJ*, **147**, 136
- Romano, D., Karakas, A. I., Tosi, M., & Matteucci, F. 2010, *A&A*, **522**, A32
- Sacchi, E., Annibali, F., Cignoni, M., et al. 2016, *ApJ*, **830**, 3
- Salpeter, E. E. 1955, *ApJ*, **121**, 161
- Sánchez Almeida, J., Elmegreen, B. G., Muñoz-Tuñón, C., et al. 2015, *ApJL*, **810**, L15
- Sánchez Almeida, J., Perez-Montero, E., Morales-Luis, A. B., et al. 2016, *ApJ*, **819**, 110
- Schlafly, E. F., & Finkbeiner, D. P. 2011, *ApJ*, **737**, 103
- Senchyna, P., & Stark, D. P. 2019, *MNRAS*, **484**, 1270
- Shibata, M., & Shapiro, S. L. 2002, *ApJL*, **572**, L39
- Shivvers, I., Modjaz, M., Zheng, W., et al. 2017, *PASP*, **129**, 54201
- Skillman, E. D., Salzer, J. J., Berg, D. A., et al. 2013, *AJ*, **146**, 3
- Storey, P. J., & Hummer, D. G. 1995, *MNRAS*, **272**, 41
- Storey, P. J., Sochi, T., & Badnell, N. R. 2014, *MNRAS*, **441**, 3028
- Sullivan, M., Le Borgne, D., Pritchett, C. J., et al. 2006, *ApJ*, **648**, 868
- Suzuki, A., & Maeda, K. 2018, *ApJ*, **852**, 101
- Takahashi, K., Yoshida, T., & Umeda, H. 2018, *ApJ*, **857**, 111
- Tayal, S. S. 2011, *ApJS*, **195**, 12
- Thuan, T. X., Lecavelier des Etangs, A., & Izotov, Y. I. 2005, *ApJ*, **621**, 269
- Totani, T., Morokuma, T., Oda, T., Doi, M., & Yasuda, N. 2008, *PASJ*, **60**, 1327
- Tumlinson, J., & Shull, J. M. 2000, *ApJ*, **528**, L65
- Umeda, H., & Nomoto, K. 2008, *ApJ*, **673**, 1014
- Vincenzo, F., Belfiore, F., Maiolino, R., Matteucci, F., & Ventura, P. 2016, *MNRAS*, **458**, 3466
- Vink, J. S. 2018, *A&A*, **615**, A119
- Wise, J. H., Turk, M. J., Norman, M. L., & Abel, T. 2012, *ApJ*, **745**, 50
- Xing, Q.-F., Zhao, G., Aoki, W., et al. 2019, *NatAs*, **3**, 631
- Xu, Y., Ouchi, M., Rauch, M., et al. 2021, arXiv:2112.08045
- Zahid, H. J., Bresolin, F., Kewley, L. J., Coil, A. L., & Davé, R. 2012, *ApJ*, **750**, 120
- Zhang, H. 1996, *AAS*, **119**, 523